

NASA/TM—2014-218337

ARL—TR—6941



The Vibration Ring

Seedling Fund Phase 1 Final Report

*Vivake M. Asnani, Timothy L. Krantz, and Damon C. Delap
Glenn Research Center, Cleveland, Ohio*

*David B. Stringer
U.S. Army Research Laboratory, Glenn Research Center, Cleveland, Ohio*

NASA STI Program . . . in Profile

Since its founding, NASA has been dedicated to the advancement of aeronautics and space science. The NASA Scientific and Technical Information (STI) program plays a key part in helping NASA maintain this important role.

The NASA STI Program operates under the auspices of the Agency Chief Information Officer. It collects, organizes, provides for archiving, and disseminates NASA's STI. The NASA STI program provides access to the NASA Aeronautics and Space Database and its public interface, the NASA Technical Reports Server, thus providing one of the largest collections of aeronautical and space science STI in the world. Results are published in both non-NASA channels and by NASA in the NASA STI Report Series, which includes the following report types:

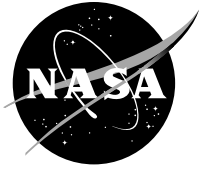
- **TECHNICAL PUBLICATION.** Reports of completed research or a major significant phase of research that present the results of NASA programs and include extensive data or theoretical analysis. Includes compilations of significant scientific and technical data and information deemed to be of continuing reference value. NASA counterpart of peer-reviewed formal professional papers but has less stringent limitations on manuscript length and extent of graphic presentations.
- **TECHNICAL MEMORANDUM.** Scientific and technical findings that are preliminary or of specialized interest, e.g., quick release reports, working papers, and bibliographies that contain minimal annotation. Does not contain extensive analysis.
- **CONTRACTOR REPORT.** Scientific and technical findings by NASA-sponsored contractors and grantees.

- **CONFERENCE PUBLICATION.** Collected papers from scientific and technical conferences, symposia, seminars, or other meetings sponsored or cosponsored by NASA.
- **SPECIAL PUBLICATION.** Scientific, technical, or historical information from NASA programs, projects, and missions, often concerned with subjects having substantial public interest.
- **TECHNICAL TRANSLATION.** English-language translations of foreign scientific and technical material pertinent to NASA's mission.

Specialized services also include creating custom thesauri, building customized databases, organizing and publishing research results.

For more information about the NASA STI program, see the following:

- Access the NASA STI program home page at <http://www.sti.nasa.gov>
- E-mail your question to help@sti.nasa.gov
- Fax your question to the NASA STI Information Desk at 443-757-5803
- Phone the NASA STI Information Desk at 443-757-5802
- Write to:
STI Information Desk
NASA Center for AeroSpace Information
7115 Standard Drive
Hanover, MD 21076-1320



The Vibration Ring

Seedling Fund Phase 1 Final Report

*Vivake M. Asnani, Timothy L. Krantz, and Damon C. Delap
Glenn Research Center, Cleveland, Ohio*

*David B. Stringer
U.S. Army Research Laboratory, Glenn Research Center, Cleveland, Ohio*

National Aeronautics and
Space Administration

Glenn Research Center
Cleveland, Ohio 44135

Acknowledgments

Support for this work was provided by the NASA Aeronautics Research Mission Directorate Seedling Fund with in-kind contributions from the U.S. Army Research Laboratory.

This report contains preliminary findings,
subject to revision as analysis proceeds.

Trade names and trademarks are used in this report for identification
only. Their usage does not constitute an official endorsement,
either expressed or implied, by the National Aeronautics and
Space Administration.

Level of Review: This material has been technically reviewed by technical management.

Available from

NASA Center for Aerospace Information
7115 Standard Drive
Hanover, MD 21076-1320

National Technical Information Service
5301 Shawnee Road
Alexandria, VA 22312

Available electronically at <http://www.sti.nasa.gov>

Contents

Abstract.....	1
Nomenclature.....	1
1.0 Introduction.....	4
2.0 Design.....	8
2.1 Preliminary Design Concepts.....	8
2.2 Detailed Designs.....	11
2.3 Damping and Power Generation Testing.....	15
3.0 Analysis.....	16
3.1 Shunted Piezo Stack Model.....	16
3.2 Vibration Ring Model.....	22
3.3 Vibration Ring Finite Element Analysis.....	28
3.3.1 Stress Analysis.....	30
3.3.2 Evaluation of Analytical Model Assumptions.....	30
3.3.3 Comparison With Analytical Model.....	34
3.4 Driveline Damping Study Using Analytical Model.....	35
3.4.4 Case 1: Variation of κ (piezo electromechanical coupling factor).....	36
3.4.5 Case 2: Variation in α (Stiffness Ratio).....	38
4.0 Conclusion.....	41
4.1 Summary.....	41
4.2 Lessons.....	42
4.3 Plans for Phase 2.....	42
References.....	43

The Vibration Ring

Seedling Fund Phase 1 Final Report

Vivake M. Asnani, Timothy L. Krantz, and Damon C. Delap
National Aeronautics and Space Administration
Glenn Research Center
Cleveland, Ohio 44135

David B. Stringer
U.S. Army Research Laboratory
Glenn Research Center
Cleveland, Ohio 44135

Abstract

The vibration ring was conceived as a driveline damping device to prevent structure-borne noise in machines. It has the appearance of a metal ring, and can be installed between any two driveline components like an ordinary mechanical spacer. Damping is achieved using a ring-shaped piezoelectric stack that is poled in the axial direction and connected to an electrical shunt circuit. Surrounding the stack is a metal structure, called the compression cage, which squeezes the stack along its poled axis when excited by radial driveline forces. The stack in turn generates electrical energy, which is either dissipated or harvested using the shunt circuit. Removing energy from the system creates a net damping effect. The vibration ring is much stiffer than traditional damping devices, which allows it to be used in a driveline without disrupting normal operation. In phase 1 of this NASA Seedling Fund project, a combination of design and analysis was used to examine the feasibility of this concept. Several designs were evaluated using solid modeling, finite element analysis, and by creating prototype hardware. Then an analytical model representing the coupled electromechanical response was formulated in closed form. The model was exercised parametrically to examine the stiffness and loss factor spectra of the vibration ring, as well as simulate its damping effect in the context of a simplified driveline model. The results of this work showed that this is a viable mechanism for driveline damping, and provided several lessons for continued development.

Nomenclature

A	Piezo element face area
c	Dynamic compliance of system
C	Piezo stack capacitance with free mechanical boundaries
d	Piezo constant of element
d_{eff}	Effective piezo constant of stack
D	Electric displacement of piezo element
E	Electric field of piezo element
f	Frequency
f_n	Natural frequency of system with vibration ring
$f_{n,b}$	Natural frequency of baseline system
F	Piezo stack force
F'	Piezo stack force with reversed sign convention (compressive force > 0)

F_{cage}	Compression cage force
F_{el}	Piezo element force
F_{ext}	Vibration ring radial force
F_{in}	System input force, applied to shaft
F_{link}	Vibration ring link force
F_{out}	System output force, transmitted to housing
FT	Force transmissibility of system
FTR	Force transfer ratio, efficiency of force transfer from vibration ring to stack
G	Function relating complex stack stiffness to complex vibration ring stiffness
H	Function relating stack short circuit stiffness to complex stack stiffness
H_n	The value of H at the system natural frequency
I	Piezo stack current
I_{el}	Piezo element current
I_L	Load current
j	Imaginary number
k	Piezo stack stiffness
\tilde{k}	Piezo stack complex stiffness
k_b	Baseline system stiffness
\tilde{k}_b	Baseline system complex stiffness
k_{cage}	Compression cage stiffness
\tilde{k}_{eff}	Effective complex stiffness of system (with vibration ring)
$k_{\text{eff},n}$	Effective stiffness of system at the natural frequency
k_n	Piezo stack stiffness at the system natural frequency
k_{oc}	Open circuit stiffness of piezo stack
k_{sc}	Short circuit stiffness of piezo stack
k_{vr}	Vibration ring stiffness
\tilde{k}_{vr}	Complex valued vibration ring stiffness
$k_{\text{vr},n}$	Vibration ring stiffness at the system natural frequency
l	Piezo element thickness
L_{link}	Length of mechanical amplifier links in vibration ring
L_{wall}	Axial length of vibration ring hoop walls
m_s	Mass of shaft
n	Number of piezo elements in a stack
P_L	Power delivered to load
R_L	Load resistance
R_L^{max}	Load resistance associated with maximum piezo stack loss factor
s^E	Elastic compliance constant of piezo element under constant electric field
S	Piezo element strain
t	Time

T	Piezo element stress
V	Piezo stack voltage
V_{el}	Piezo element voltage
w	Distance between inner and outer vibration ring links
W_1	Electric energy delivered to load during electromechanical coupling virtual experiment
W_2	Mechanical energy recovered during electromechanical coupling virtual experiment
W_d	Energy dissipated per steady state oscillation cycle of a complex spring
W_{tot}	Total steady state oscillation energy of a complex spring
x	Radial compression of vibration ring wall
x_{unload}	Unloaded radial distance between inner and outer walls of vibration ring
x_{load}	Loaded radial distance between inner and outer walls of vibration ring
x_s	Shaft displacement
y	Piezo stack displacement
y'	Piezo stack displacement with reversed sign convention (compression > 0)
y_{el}	Piezo element displacement
y_{unload}	Unloaded height of piezo stack
y_{load}	Loaded height of piezo stack
y_{max}	Maximum stack displacement in the electromechanical coupling factor virtual experiment
z_L	Load impedance
α	Ratio of cage stiffness to vibration ring stiffness
β	Ratio of system natural frequencies with and without vibration ring
ϵ^T	Permittivity constant of piezo element under constant stress
η	Piezo stack loss factor
η^{max}	Maximum loss factor of piezo stack
η_b	Loss factor of baseline system
η_{vr}	Vibration ring loss factor
η_{vr}^{max}	Maximum loss factor of vibration ring
κ	Piezo stack electromechanical coupling factor
κ_{el}	Piezo element electromechanical coupling factor
ϕ_{unload}	Unloaded vibration ring link angle
ϕ_{load}	Loaded vibration ring link angle
ω	Angular frequency

1.0 Introduction

Rotating machines create noise with levels ranging from unpleasant to damaging. The main noise sources are high speed driveline components, such as gears, bearings, shafts, fans, etc. These parts create periodic forces, which shake the machine body and generate structure-borne noise. The example that motivated this work was the environment within the cabin of a rotorcraft. Here the driveline-induced noise exceeds 100 dB, making it impossible to communicate without headsets. This environment creates pilot fatigue and limits the commercial use of rotorcraft for civilian transportation. As a part of the National Aeronautics Research and Development Plan, the United States set the goal to reduce main rotor gearbox noise by 20 dB (National Science and Technology Council, 2010).

Structural damping is the most common method to reduce machine noise, accomplished by applying hysteretic material (like rubber) to the radiating surfaces. As the surfaces move, work is done on the material, which removes part of the energy in the form of heat. For rotorcraft this approach is limited, because it would require too much added mass to effectively dampen the cabin walls. This shortcoming motivates the present investigation to develop a damper that would reduce vibration energy within the driveline. The idea is conceptually illustrated in Figure 1 using the case of a simple gearbox. Here dampers have been placed around the shaft bearings to reduce the amount of vibration energy transferred to the gearbox housing and to the rest of the machine.

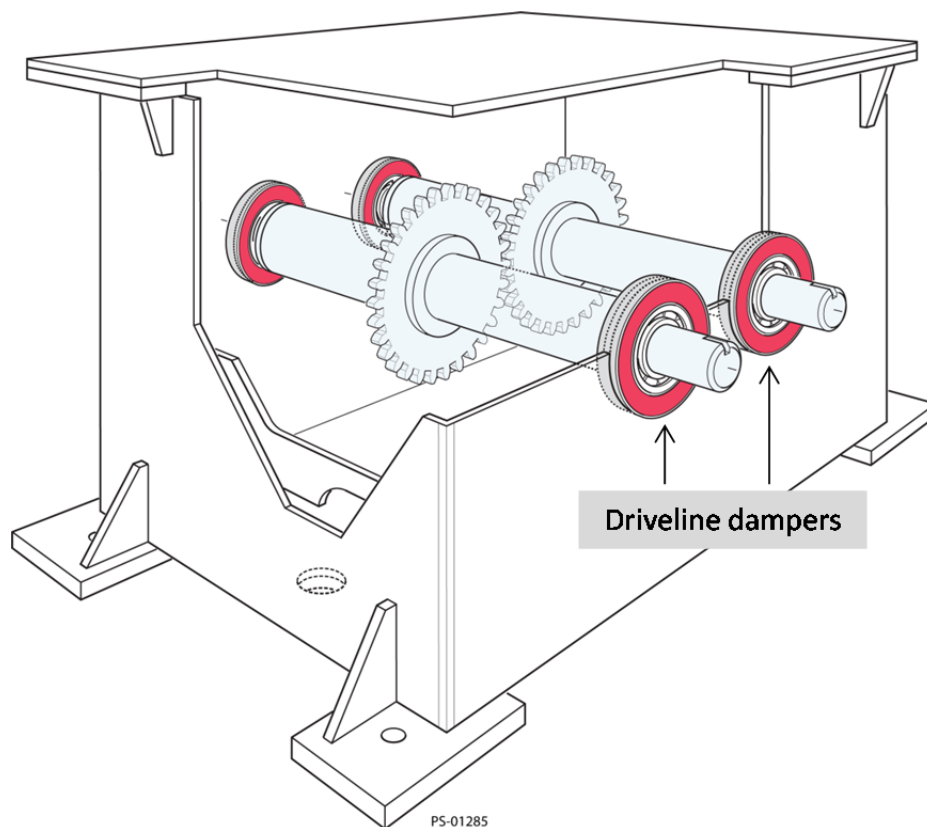


Figure 1.—Concept drawing of driveline dampers mounted around the shaft bearings of a gearbox. The dampers reduce the driveline vibration and in-turn lower the amount of energy transferred through the gearbox housing to the rest of the machine.

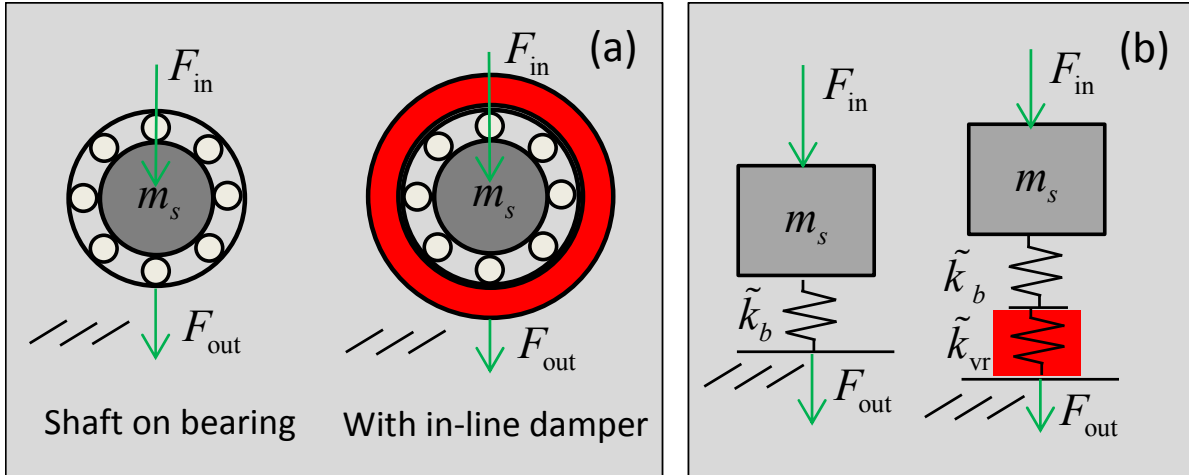


Figure 2.—Simple driveline with and without in-line damper. (a) Schematics, (b) Analytical models.

The damper was envisioned to have a simple ring-shaped geometry, allowing it to be placed in-between any two driveline components (e.g., between a gear/shaft or bearing/housing). In-line damping devices are not typical, because they alter the frequency response of the original system. To gain some intuition for how to best configure such a device, consider the simplified driveline schematic in Figure 2(a). On the left is a shaft supported by a bearing within a mechanical housing. On the right, is the same system including the subject in-line damper. Also depicted are analytical models, in Figure 2(b). Here the shaft is represented by a mass and the bearing and damper are represented by springs with stiffness (k) and loss factor (η) parameters, define as follows.

$$\tilde{k}_b = k_b (1 + j\eta_b) \quad (1)$$

$$\tilde{k}_{vr} = k_{vr} (1 + j\eta_{vr}) \quad (2)$$

The series combination of springs is expressed as,

$$\tilde{k}_{eff} = \frac{\tilde{k}_b \tilde{k}_{vr}}{\tilde{k}_b + \tilde{k}_{vr}}. \quad (3)$$

To compare these two driveline cases, the metric of force transmissibility (FT),

$$FT = \frac{F_{out}}{F_{in}} = \frac{\tilde{k}_{eff}}{-(2\pi f)^2 m_s + \tilde{k}_{eff}}, \quad (4)$$

is used to express the transfer of force from the shaft to the housing in the frequency domain. The results are plotted in Figure 3. With no damper, there is a sharp peak in the FT at the natural frequency. As shown in Figure 3(a), the peak is reduced by lowering the damper stiffness; however, this simultaneously reduces the natural frequency. To avoid drastic frequency shifts, the damper must be significantly stiffer than the bearing. Figure 3(b) shows the case where the damper stiffness is fixed at two times the bearing stiffness and the loss factor is varied. Here, it's evident that increasing the loss factor provides the desired damping effect without substantial frequency-shift.

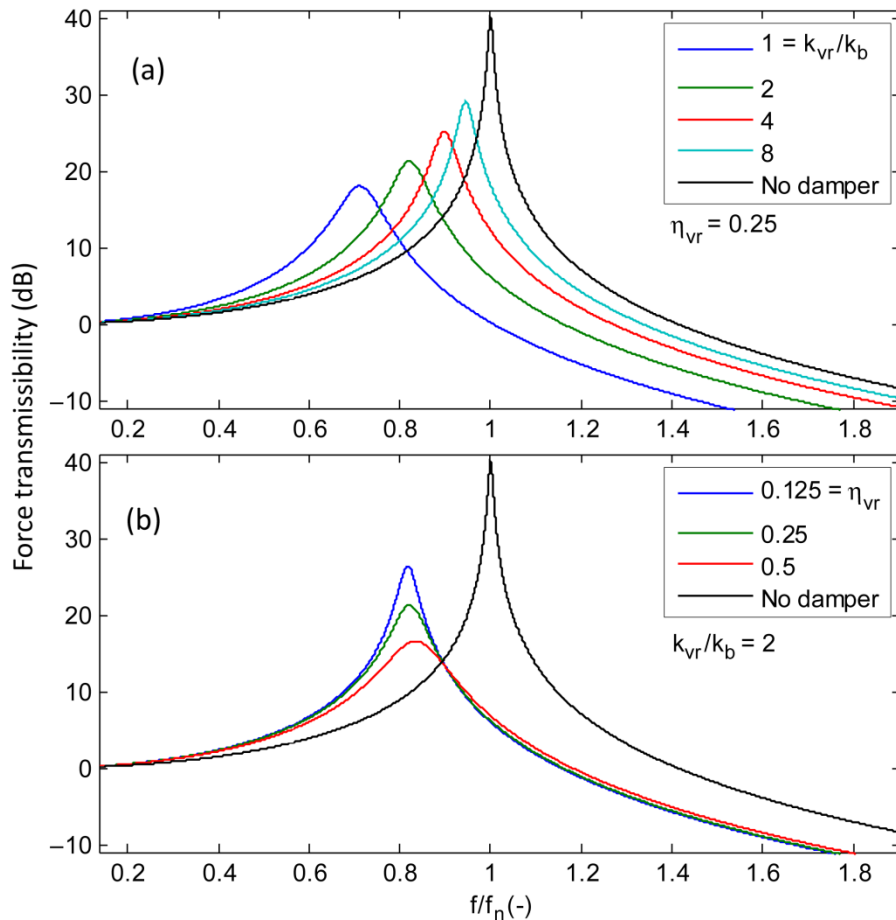


Figure 3.—Force transmissibility plots showing effects of an in-line damper. (a) Effect of varying damper stiffness with a constant damper loss factor. (b) Effect of varying damper loss factor with a constant damper stiffness.

Traditional damping materials, such as rubber, exhibit high loss factor but are far too soft to be placed in-series with steel driveline components. Shunted piezoelectric (piezo) stacks (Hagood & von Flotow, 1991) were found to be a suitable alternative. Piezo stacks are essentially multilayer piezo devices, which generate significant electric charge in response to applied vibratory force. By shunting their electric terminals the generated electrical energy is removed from the system to create a net damping effect. When used in compression they have an elastic modulus comparable to steel with loss factor comparable to rubber. There are also a few practical limitations associated with the technology. The damping effect is primarily limited to the axis in which the stacks were electrically poled. Piezo stacks have high compressive strength along their poling axis, but are relatively fragile when stressed in tension or shear.

A survey of the literature revealed that shunted piezo stacks have been experimentally evaluated for in-line driveline damping, as reported in (Atzrodt, Mayer, & Melz, 2009). The test setup consisted of a single shaft supported by a bearing, as illustrated in Figure 4. Four piezo stacks were placed in-between the bearing and mechanical housing, and each was electrically shunted by a resonant circuit. Radial vibratory force was applied to the shaft using a shaker, and the resulting shaft velocity response spectrum was examined. Engaging the resonant circuits reduced the response at the natural frequency by 17.5 dB. This result provides strong support for the use of shunted piezo stacks. However, this particular stack arrangement appears to be limited to use between a bearing and housing. On a rotating part the loads would be distributed, requiring the use of numerous stacks to create an even reaction. In addition, torque would be transferred through the stacks creating the potential for shear failure.

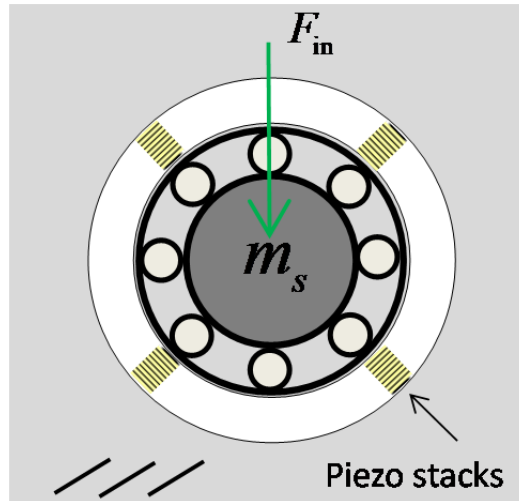


Figure 4.—Depiction of piezo shunt damping experiment reported in (Atzrodt, Mayer, & Melz, 2009).

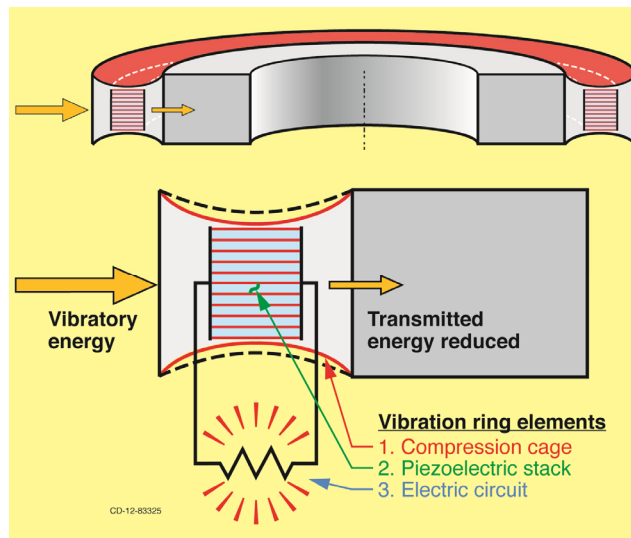


Figure 5.—Original concept drawing of the vibration ring.

The vibration ring was conceived as a mechanism to implement piezo shunt damping anywhere within the driveline. As depicted in Figure 5, it's shaped like a ring and could be installed between any two driveline components like an ordinary mechanical spacer. Instead of using radially oriented piezo stacks, a single ring-shaped stack is used. Radial force applied to the mechanism at any position is transferred to the stack through the compression cage. This generates charge in the stack, which is dissipated by the electric circuit to create the damping effect. The compression cage is the key to this innovation. It has a unique concave structure that squeezes the piezo stack in the axial direction when the inner and outer walls of the vibration ring are moved closer together. The compression cage also holds the stack under a compressive preload, and effectively shunts torque, to protect the stack from potentially damaging tensile and shear forces.

This new vibration control mechanism is being evaluated in a two-phase project supported by NASA's Aeronautics Research Mission Directorate Seedling Fund. This report provides a comprehensive record of phase 1, where the feasibility of vibration ring was examined through a combination of design and analysis.

2.0 Design

Preliminary design work focused on finding a suitable compression cage structure. Several iterations of solid modeling and rapid prototyping were done to find a concept that effectively converted radial motion into axial motion, and could also be manufactured and assembled. Once a basic understanding of the design challenges was reached, rough guidelines were formulated to provide more structure to the design process. Subsequent design concepts were developed with more detail, including finite element analysis (FEA) and complete prototype development. Test hardware was also created to evaluate the damping properties and power generation of the prototypes.

2.1 Preliminary Design Concepts

Though there were several preliminary designs created, only select concepts are discussed here to emphasize lessons learned or to provoke further consideration. As a first step in the design process, several piezo device manufacturers were contacted to find a ring-shaped piezo stack. Most offered to manufacturer custom designs, but none had this stack geometry available as an off-the-shelf product. One company provided a set of piezoceramic rings, shown in Figure 6(a), as building blocks to create a stack in-house. A second company suggested combining several commercially available linear stacks using metal rings or “stack rings”, such as in Figure 6(b). The preliminary vibration ring design concepts were based on the geometry of the piezoceramic rings. The rings were found to be too small to be practical, so the detailed designs discussed in the subsequent section made use of the stack-ring concept. This is considered a temporary solution until a suitable ring-shaped stack can be procured.

Concept 1 (Con1) was created to mimic the original depiction of the vibration ring. As shown in Figure 7, a solid model of the compression cage and corresponding plastic prototype were made. The cross section of the compression cage looked like a set of wings, and so this profile was given the name ‘butterfly amplifier’. By squeezing the walls of the plastic prototype at the open end the axial compression action of the butterfly amplifier could be observed. One of the major issues identified was that the design required significant axial width to accommodate the stack and the butterfly wings. To illustrate this, the model and prototype are shown in the figure with two bearings stacked axially.

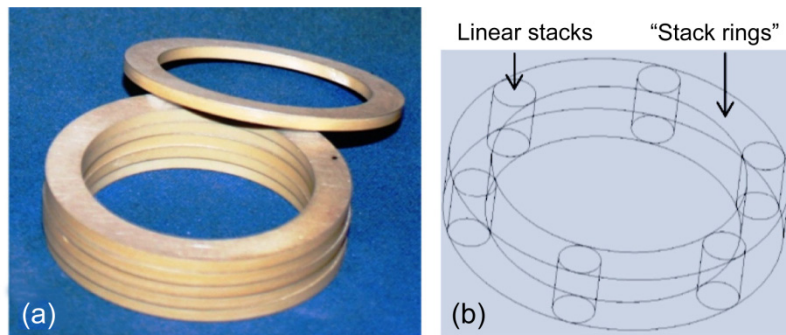


Figure 6.—Stack options. (a) Piezoceramic rings, (b) Stack ring concept.

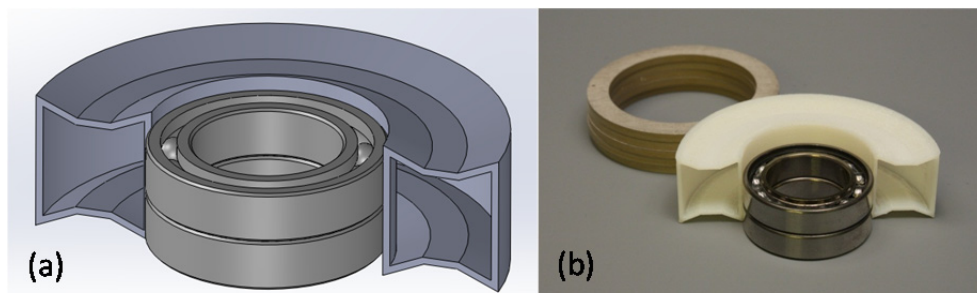


Figure 7.—Con1. (a) Solid model, (b) Plastic prototype.

Subsequent attempts were made to redesign the compression cage, so that it could be assembled around the stack. However, none of the ideas evaluated were practical. In Con6 a temporary solution was implemented so that other aspects of the design could start to be explored. The solid model is shown in Figure 8(a) and corresponding plastic prototype in Figure 8(b). Here, the compression cage was made in two axial pieces that were assembled around the stack using small bolts. Unlike Con1, the plastic cage parts felt rigid and the compression action could not be observed. The difference was that Con1 was cut along its cross-section allowing for more freedom of movement at the boundary. This led to the realization that the compression cage needed to be segmented circumferentially to function correctly.

It was felt that additive manufacturing would have some advantages for developing metal prototypes of the compression cage. The prototypes could be made directly from solid models (without drawings). Also, the compression cage could be built with complex 3D geometry that would otherwise be impractical to machine. To begin exploring this approach, the Con6 compression cage was built out of stainless steel using the direct metal laser sintering (DMLS) process, as well as by investment casting. One piece of each cage structure is shown in Figure 9. The DMLS part was found to be more precise than the casting. However, the casting had smoother surfaces and less porosity. The relative porosity of the parts was inferred, as the DMLS part was lighter and had a lower frequency acoustic response when struck.

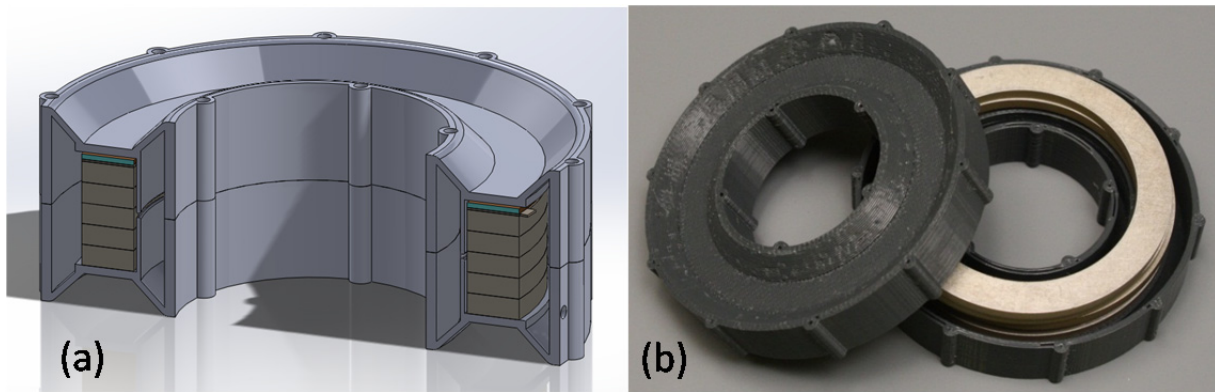


Figure 8.—Con6. (a) Solid model, (b) Plastic prototype.

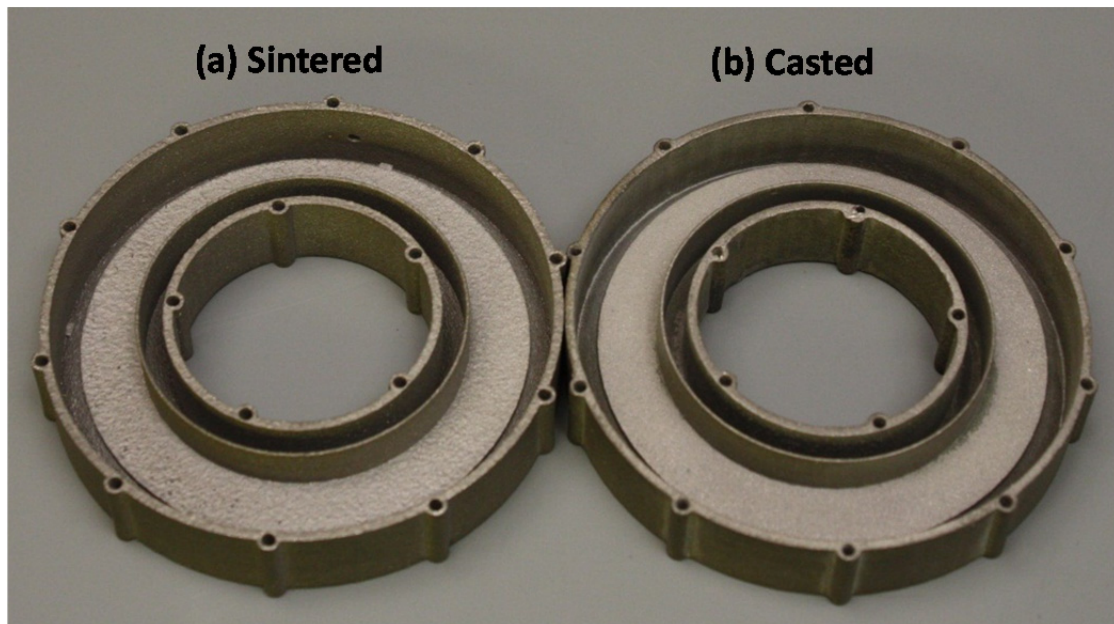


Figure 9.—Con6 stainless steel parts. (a) Sintered, (b) Casted.

Con8 and 9 did not contribute directly to the development of the more advanced designs, but they are discussed here to highlight specific features. Con8, illustrated in Figure 10, was a first attempt at creating a segmented cage. For each segment, the inner and outer wings were separate parts. Theoretically the compression cage could be assembled around the ring-shaped stack using a simple three-step process. First, two metal rings would be placed above and below the stack. Second, each wing segment would be inserted radially into slots in the metal rings. Third, the inner and outer hoops would be slid onto the design axially.

Con9, as shown in Figure 11, used an expanding form of the compression cage structure that was totally different than the other concepts. The first version, Con9a, is shown in Figure 11(a). The green section provided the amplifier action. Both the external and internal vertical members have a c-shape to them, but with different degrees of curvature. Radial deformation of the external member is transferred to the internal member through a rigid link. The internal member in turn straightens and compresses the stacks that are above and below it. Con9b, shown in Figure 11(b), was a symmetric version of this design that also had flat external surfaces for mating with other parts. The expanding structure of Con9 was interesting, but it required more axial width than the butterfly amplifier, it did not have an assembly solution, and it did not appear to offer any performance benefits to justify further investigation.

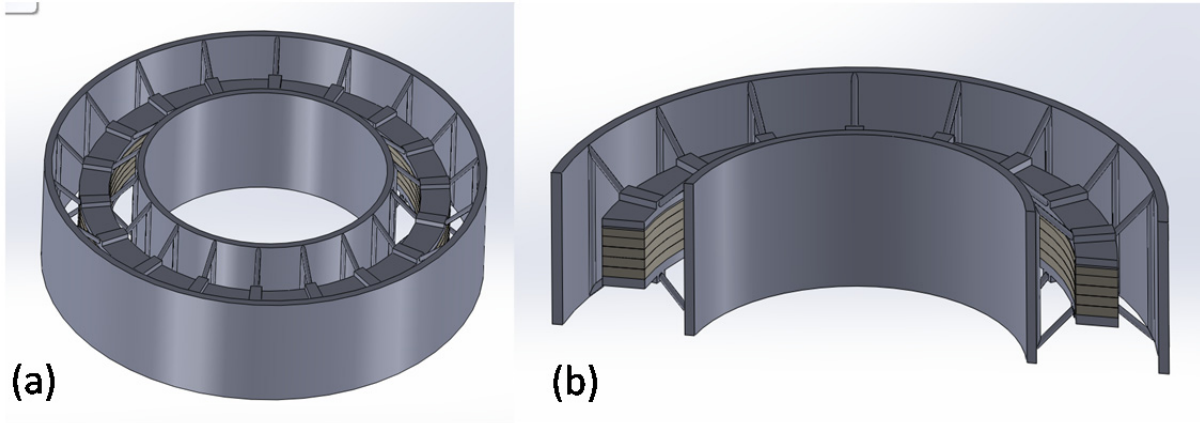


Figure 10.—Con8. (a) Overview, (b) Section view.

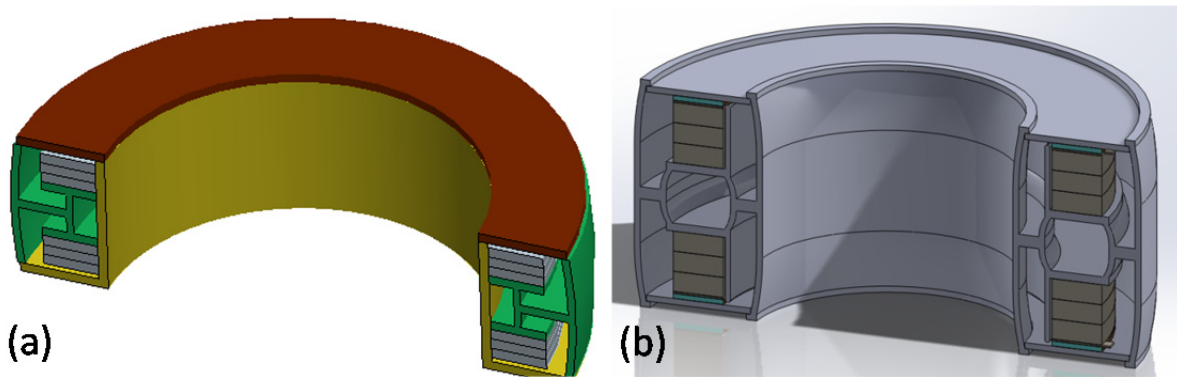
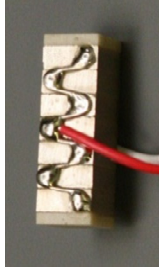


Figure 11.—Con9 solid models. (a) Con9a, (b) Con9b.

TABLE 1.—DESIGN SPECIFICATIONS

External dimensions	ID = 52 mm OD < 86 mm Axial width 15 to 30 mm	 <p>Photograph of stack</p>
Load	Radial compression Nominal 400 N Maximum 845 N	
Stack type	Noliac piezoceramic stack NAC2013-H16-A01 Height 15.8 mm Face 5.0 by 5.0 mm	
Static FEA performance criteria	Maximize the force transfer ratio at nominal load	

2.2 Detailed Designs

After evaluating the preliminary concepts, the lessons-learned were applied to create more detailed and functional designs. The new designs used the butterfly amplifier with a segmented configuration. Also, the stack-ring concept from Figure 6(b) was implemented as a temporary substitution for a ring-shaped stack. Specifications for the external dimensions, load, stack type, and FEA performance criteria were established, as listed in Table 1. In anticipation of future system level testing, the dimensions and load specifications were made to correspond to specific driveline test rigs at NASA. For this preliminary work, only compressive radial loads were considered. The stack type and FEA criteria were chosen using guidance from the analytical framework. For damping at the stack level, a high electromechanical coupling factor was shown to be essential (Eq. (31)). The specified stack was selected because it had a relatively high value (0.72) amongst commercially available products. To transfer the stack damping properties to the vibration ring, the framework showed that the ratio of cage stiffness to vibration ring stiffness needed to be minimized (Eq. (50)). As a means to achieve this goal indirectly, the FEA performance specification called for maximizing the force transfer ratio (Eq. (53)) between the vibration ring and stack. It should be noted that only static FEA was implemented for this tuning process.

Con10 is illustrated in Figures 12 to 14. This design had few parts, but required additive manufacturing to be created. Static FEA was used to evaluate the loaded response, in terms of stiffness, force transfer ratio, and stress. This is described in detail in the analysis section of this report. The first version, Con10a, is shown in Figure 12. It used nine stacks and had four sections: Top and bottom pieces to the cage structure, as well as inner and outer hoops. To assemble this design, the bottom cage section would be bolted to the inner and outer hoops, the stacks would be inserted and then the top section would be bolted into position. FEA results showed that the maximum stress was highly dependent on the link radii and thickness, and that the design would be overly sensitive to fabrication error. This was attributed to the tight radius in the butterfly wing, as annotated in Figure 12(b). In addition, the bolt clearances were considered to reduce assembly precision.

Con10b was a modified version, intended to overcome the limitations. It was a two piece structure consisting of the main compression cage section, shown in Figure 13(a), and an outer hoop (not shown). The piezo stacks were intended to be inserted radially, the hoop would be slid around the structure, and then countersunk screws would be used to precisely fasten the two members. Relative to Con10a, the fasteners were located further outboard to eliminate the tight radius in the butterfly wing. This design was still somewhat sensitive to link geometry, and so the DMLS process was selected over investment casting to create the prototype.

All of the thin stainless steel sections for Con10b were severely warped by heat in the DMLS process. To allow the parts to mate together, quite a bit of final machining and bending of the parts needed to be done. Shims were then inserted to apply preload to the stacks. The final prototype is illustrated in Figure 14.

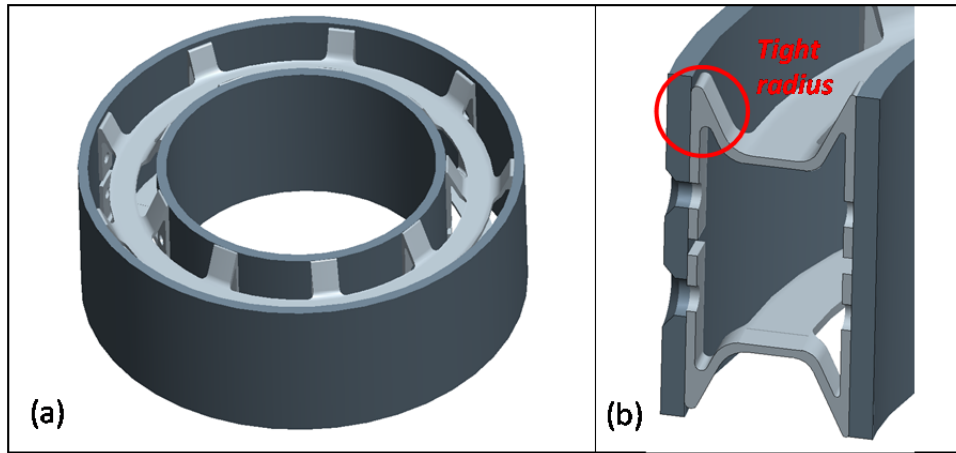


Figure 12.—Con10a solid model. (a) Overview, (b) Cross section.

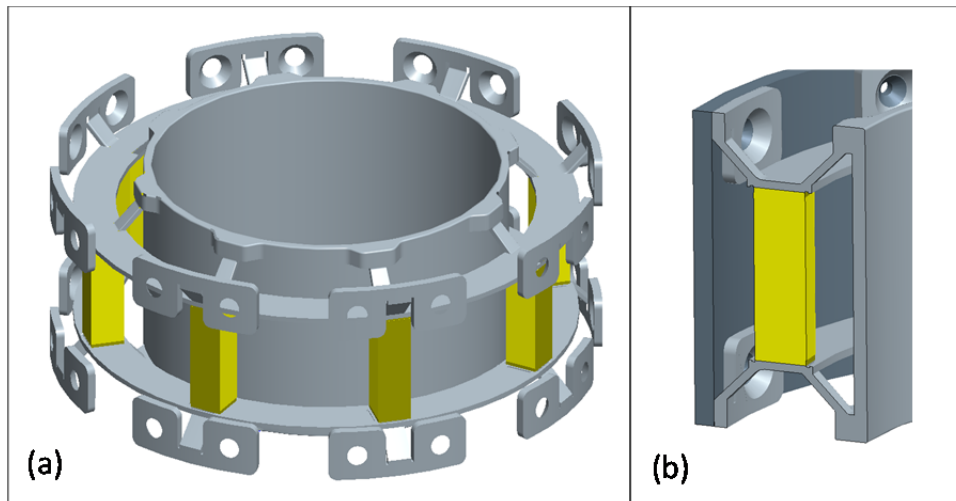


Figure 13.—Con10b solid model. (a) Main compression cage section, (b) Cross section.

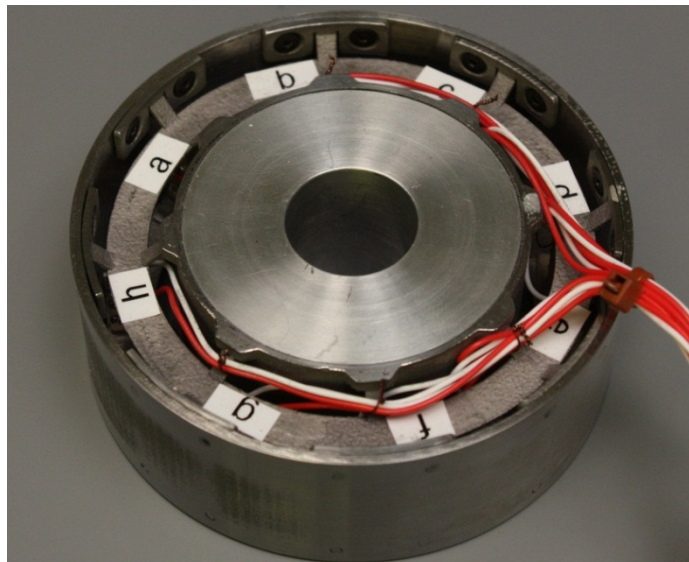


Figure 14.—Con10b prototype created by DMLS. Shown with an aluminum mounting fixture inside.

Con11, shown in Figures 15 to 18, was developed to improve the prototype precision by using more conventional manufacturing processes. The first iteration, Con11a, is illustrated in Figure 15. Instead of having a unified cage structure, there were several separate parts that could be made using a combination of wire electrical discharge machining, milling, and turning. The parts installed axially, and were loaded against metal tabs on each side. A couple of additional special features were added to make assembly easier. First, the links were notched in the center, so they could be folded slightly and inserted between the inner and outer hoops. Once in place, the links would be released and would expand into small pockets in the hoop walls. The pockets were essentially a locating feature. The stack cap part would fill the notch in the link, like a tongue-in-groove arrangement. Second, set screws were included in the tabs to hold the assembly in place, and apply preload to the stacks.

The pocket and tongue and groove features of Con11a were thought to complicate fabrication, and so Con11b was created without these features. As illustrated in Figure 16, the design was otherwise very similar to Con11a. One notable change was that the stack rings were placed outside of the links to allow them to be removed. This provided the option to measure their influence on performance.

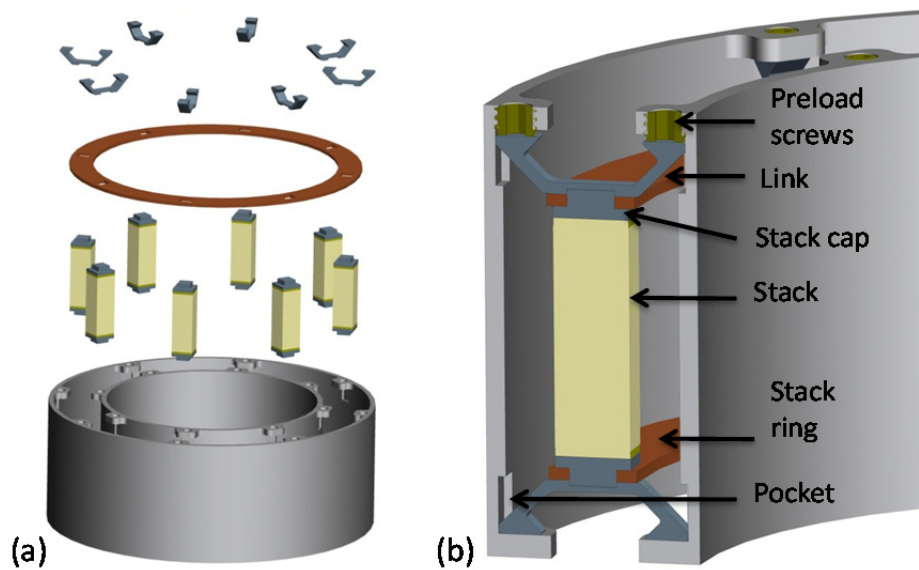


Figure 15.—Con11a solid model. (a) Exploded view, (b) Cross section.

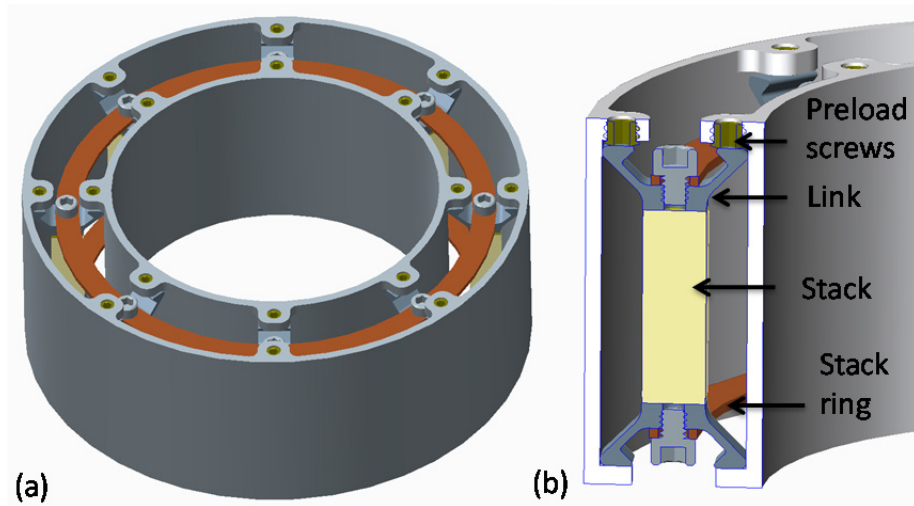


Figure 16.—Con11b solid model. (a) Overview, (b) Cross section.

Manufacturing of the Con11b prototype was fairly straightforward. There were no issues with tolerances or warped parts. However, assembly was more difficult than anticipated. Two pictures from the assembly process are included in Figure 17, for reference. The main issue was that the interference fit between the links and hoops made it so the parts needed to be forced into position. To install the final links, the hoop walls needed to be pried apart, as illustrated in Figure 17(b). After all of the parts were installed, the inner and outer hoops were slightly offset in the axial direction. This occurred, because the links had rotated to relieve their interference fit. To correct this, a mechanical press was used force the inner hoop back into alignment with the outer hoop. Once in position, the set screws were tightened to establish preload on the stacks. The final prototype assembly is shown in Figure 18.

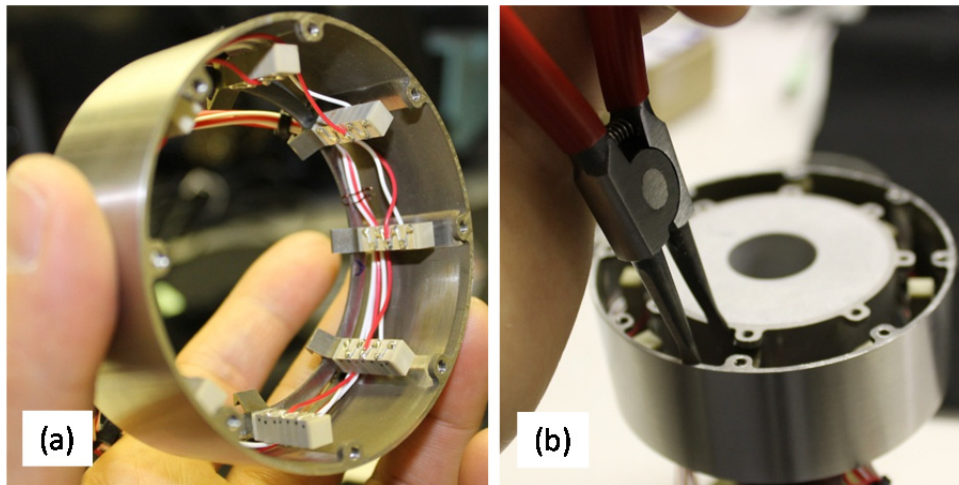


Figure 17.—Con11b prototype. (a) Partial assembly, (b) Separating hoops to insert link.

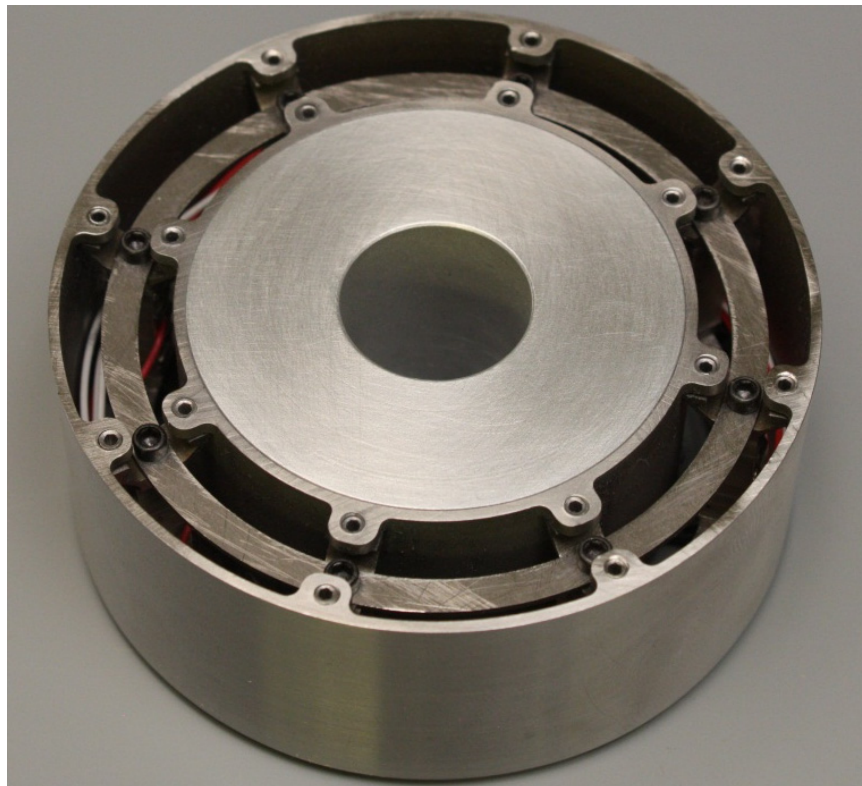


Figure 18.—Con11 prototype. Shown with an aluminum mounting fixture inside.

2.3 Damping and Power Generation Testing

Based on the analytical work presented in the next section of this report, a method and metrics were developed to assess the stiffness, damping, and power generation of the vibration ring prototypes. Testing is being done using the high speed load frame illustrated in Figure 19(a). This system is typically used for elastomer testing and has the capability to apply controlled vibratory loads up to 1000 Hz. For this work, the system was augmented to include a data acquisition system to acquire high speed and high voltage sensor signals. A test fixture, shown in Figure 19(b), was built to hold the vibration ring during testing and rotate its orientation. The fixture includes a load cell to measure the applied force and nano-precision displacement probes to observe deformation. The piezo stacks are wired to external shunt circuits, which provide access points to measure voltage. The force, displacement, and circuit voltages are acquired by the data acquisition system. Preliminary data was gathered in phase 1 of the project, but it was not until phase 2 that systematic testing methods were established. Therefore, the performance data for all prototypes will be presented together in the phase 2 report.

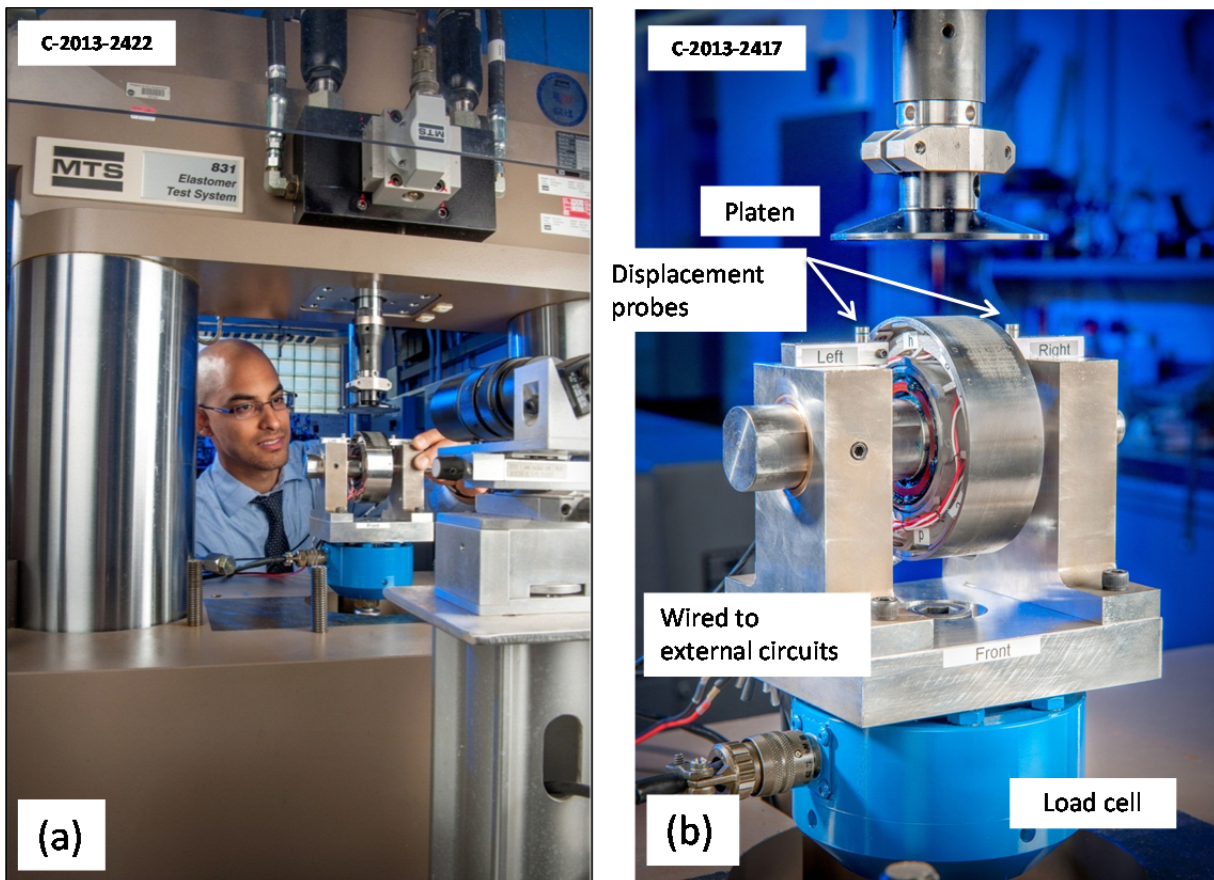


Figure 19.—Test setup. (a) Load frame, (b) Test fixture.

3.0 Analysis

In this section, a 2D analytical model is created to represent the dynamic electro-mechanical response of the vibration ring in closed form. The compression cage, piezo stack, and electric circuit features are related to the frequency-dependent stiffness and loss factor of the vibration ring. FEA is used to evaluate the analytical model assumptions and to provide greater insight about the mechanism. The analytical model is then used to study how the vibration ring parameters relate to damping performance using the previously introduced driveline model.

3.1 Shunted Piezo Stack Model

As a first step, the shunted piezo stack is formulated as a complex spring, so it may be incorporated with the mechanical framework of the vibration ring. Relationships are also derived that allow for the stack damping to be maximized and for power generation to be predicted. Such equations may be found in various forms in the technical literature (e.g., (Hagood & von Flotow, 1991)). Nonetheless a complete and systematic development is presented here to provide insight. For reference, the scope and assumptions of the model are listed in Table 2.

TABLE 2.—SCOPE AND ASSUMPTION OF THE SHUNTED PIEZO STACK MODEL

1	Each element of the piezo stack is modeled using the linear constitutive equations of piezoelectricity (ANSI, 1987). Therefore nonlinear effects are not considered.
2	Only the motion along the stack's poling axis (the 3-axis) is described and so numerical subscripts designating the input and output variable orientations have been omitted.
3	Unless otherwise stated, waveforms are represented by phasors with the following convention. Results are therefore indicative of steady state response to sinusoidal type excitation. $y(t) = y_o \cos(\omega t + \phi_y) = \text{Re}\{y e^{j\omega t}\} \Rightarrow y = y_o e^{j\phi_y} \quad (5)$
4	Electric charge leakage and mechanical hysteretic losses are neglected.
5	When relating properties of the piezo elements to stack properties, the following assumptions are made: a) Stress and charge are assumed to be evenly distributed across the face area of each element. b) Strain and electric field are assumed to be uniformly distributed through the thickness of each element. c) The compliance of the insulating end-plates and electrodes/glue between elements are neglected. d) The in-plane constraints created by bonding the elements are not taken into account. However, when the model is parameterized based on measured piezo stack data these assumptions are not required.

Considering a single piezo element, the linear constitutive matrix equation for electro-mechanical coupling (ANSI, 1987) is,

$$\begin{bmatrix} S \\ D \end{bmatrix} = \begin{bmatrix} s^E & d \\ d & \varepsilon^T \end{bmatrix} \begin{bmatrix} T \\ E \end{bmatrix}. \quad (6)$$

The equation represents mechanical strain, S , and electric displacement, D , as functions of applied mechanical stress, T , and electric field, E . The relationships are governed by the element's elastic compliance constant, s^E , permittivity constant, ε^T , and its piezo constant, d . The compliance constant has the superscript E to designate that it was measured under a condition of constant electric field (i.e., when the electrodes were shorted). The permittivity constant has the superscript T to designate that it was measured under a condition of constant stress (i.e., with free mechanical boundaries). The piezo constant represents the special property of piezo materials, which allows for stress to cause electric displacement and electric field to cause strain. By assuming that the stress and charge are evenly distributed across the element's face area and that the strain and electric field are uniformly distributed through the element thickness, the following change of variables is made,

$$\begin{bmatrix} y_{el}/l \\ I_{el}/j\omega A \end{bmatrix} = \begin{bmatrix} s^E & d \\ d & \varepsilon^T \end{bmatrix} \begin{bmatrix} F_{el}/A \\ V_{el}/l \end{bmatrix}. \quad (7)$$

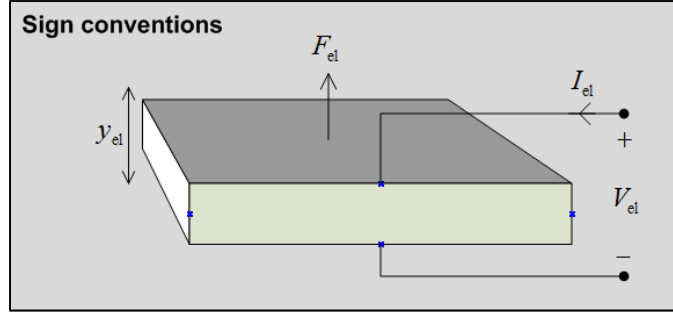


Figure 20.—Sign conventions for piezo element variables.

The output variables have become displacement, y , and current, I , while the input variables are force, F , and voltage, V . The geometric factors, A and l , are the element's face area and thickness. The subscript el is used to distinguish the elemental quantities represented here from those associated with a complete stack. To clarify the sign conventions, Figure 20 shows the input and output variables with respect to an element.

For a typical piezo stack, several elements are connected in a mechanical series, but with their electrodes connected in parallel. The combination of n -elements into a stack is mathematically described by the following equations:

$$F = F_{el}, y = ny_{el}, V = V_{el}, I = nI_{el}. \quad (8)$$

The variables listed without subscripts are associated with the complete stack, rather than a single element. Using the above transformations, Equation (7) is rewritten as,

$$\begin{bmatrix} y \\ I/j\omega \end{bmatrix} = \begin{bmatrix} \frac{nls^E}{A} & nd \\ nd & \frac{nA\epsilon^T}{l} \end{bmatrix} \begin{bmatrix} F \\ V \end{bmatrix}. \quad (9)$$

The following approximations are then introduced to relate the element properties to the stack properties,

$$k_{sc} = \frac{A}{nls^E}, C = \frac{nA\epsilon^T}{l}, d_{eff} = n \cdot d \quad (10)$$

Here k_{sc} is the short-circuit stiffness or the stiffness when the electrodes of the stack are shorted together and C is the stack capacitance when the stack ends are mechanically unconstrained. The factor d_{eff} is the effective piezo constant of the stack, which relates voltage to displacement when the stack ends are mechanically unconstrained as well as relating force to charge ($I/j\omega$) when the electrodes are shorted together. It should be noted that the short-circuit stiffness equation does not take into account the compliance of the insulating end-plates or electrodes/glue between the stack elements. The bonding layers between elements also impose in-plane constraints that have not been considered. Therefore these equations must be viewed as approximations. Applying the transformations leads to the following set of equations.

$$y = \frac{F}{k_{sc}} + d_{eff}V \quad (11)$$

$$\frac{I}{j\omega} = d_{\text{eff}}F + CV \quad (12)$$

These are the most basic linear equations of a piezo stack, which indicate how force or voltage gives rise to displacement and charge. The following equation is introduced to represent the connection of a shunt circuit to the electrodes.

$$I_L = \frac{V}{z_L} = -I \quad (13)$$

Here z_L is the load impedance and I_L is the current flowing into the load. Equation (13) is inserted into Equation (12) to produce expressions for generated voltage and power delivered to the load in response to applied force.

$$V = \frac{-d_{\text{eff}}F}{C + 1/j\omega z_L} \quad (14)$$

$$P_L = V^2/z_L \quad (15)$$

Inserting Equation (14) into (11), and solving for F/y , leads the following equation representing the complex valued stiffness of the stack.

$$\tilde{k} = \frac{1}{\frac{1}{k_{\text{sc}}} - \frac{d_{\text{eff}}^2}{C + 1/j\omega z_L}} \quad (16)$$

The complex valued stiffness carries information about both stiffness and damping, as will be explained later in this formulation. As shown by the equation, its value depends on the electrical impedance. The minimum value is the short circuit stiffness k_{sc} , which corresponds to load impedance $z_L = 0$. The maximum value, called the open circuit stiffness, corresponds to $z_L = \infty$, and is defined by,

$$k_{\text{oc}} = \frac{1}{\frac{1}{k_{\text{sc}}} - \frac{d_{\text{eff}}^2}{C}} \quad (17)$$

The electromechanical coupling coefficient, κ , is now introduced to simplify the complex stiffness equation. This variable was defined in (ANSI, 1987) as a dimensionless material property, relating the electrical energy generated to the mechanical energy applied. This definition is extended to a piezo stack by examining the conceptual energy conversion experiment illustrated by Figure 21. The experiment has three phases: (1) Force is applied in absence of an electrical load, requiring the applied energy to be stored within the stack. (2) The displacement is fixed, while a low impedance electrical load is connected and the electrical energy is drained. Due to the piezo effect, this causes a reduction in force magnitude. (3) With the electrical load in place, the piezo is returned to zero displacement.

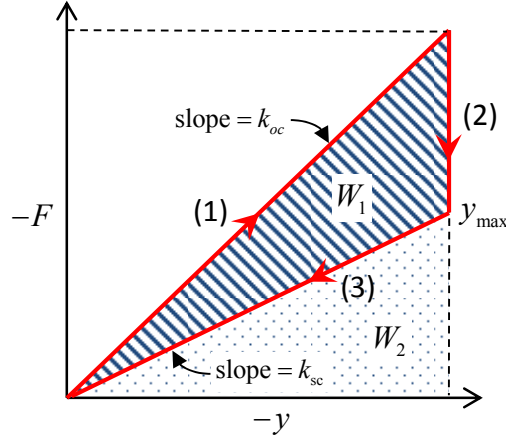


Figure 21.—Conceptual experiment to measure piezo energy conversion.

Assuming no losses within the piezo stack, the electrical energy delivered to the load is W_1 and the applied mechanical energy is $W_1 + W_2$. The coupling factor, defined in terms of energy, is therefore related to the open and short circuit stiffness quantities as shown below.

$$\kappa^2 := \frac{W_1}{W_1 + W_2} = \frac{\frac{y_{\max}^2}{2} (k_{oc} - k_{sc})}{\frac{y_{\max}^2}{2} k_{oc}} = 1 - \frac{k_{sc}}{k_{oc}} \quad (18)$$

Based on this equation, measurements of short and open circuit stiffness may be used to indirectly find the coupling coefficient. The more common expression for the coupling coefficient, shown below, is found by inserting Equation (17) into (18).

$$\kappa^2 = \frac{d_{\text{eff}}^2 \cdot k_{sc}}{C} \quad (19)$$

Inserting Equation (19) into (16) leads to the following expression for complex stack stiffness.

$$\tilde{k} = k_{sc} H, \quad H = 1 + \frac{\kappa^2}{1 - \kappa^2 + \frac{1/j\omega C}{z_L}} \quad (20)$$

Note that Equation (20) was previously derived and presented in (Davis & Lesieutre, 2000). With this representation it's clear that complex stiffness is controlled by the impedance ratio between the piezo capacitance and the load. To separate the complex valued stiffness into lossless stiffness, k , and loss factor, η , the following expansion is applied.

$$\tilde{k} = k[1 + j\eta], \quad (21)$$

The derivation of this relationship, originally presented by (Ungar & Kerwin Jr., 1962), is examined here to clarify the meaning of k and η . Consider Hook's law for a complex valued spring,

$$F = \tilde{k}y = k[1 + j\eta]y. \quad (22)$$

The following is the equivalent expression in the time domain,

$$\frac{F(t)}{k} = y(t) - \eta y_o \sin(\omega t + \phi_y). \quad (23)$$

By applying Pythagorean's trigonometric identify this becomes,

$$\frac{F(t)}{k} = y(t) \pm \eta \sqrt{y_o^2 - y_o^2 \cos^2(\omega t + \phi_y)}. \quad (24)$$

Inserting the phasor definition of $y(t)$ from Equation (5) leads to the following relationship between force and displacement.

$$\frac{F(t)}{k} = y(t) \pm \eta \sqrt{y_o^2 - y^2(t)} \quad (25)$$

The equation shows that when $\eta = 0$ the relationship between force and displacement is that of an ordinary spring with spring constant k . Thus, k is the lossless component of the complex stiffness. Plots of Equation (25) in Figure 22 illustrate that finite values of η create a hysteresis loop in the relationship between force and displacement. Considering steady-state oscillation, the energy dissipated per cycle may be calculated based on the energy input per cycle as follows.

$$\begin{aligned} W_d &= \oint F[y(t)] dy \\ &= k \int_{-y_o}^{y_o} y(t) + \eta \sqrt{y_o^2 - y^2(t)} dy - k \int_{-y_o}^{y_o} y(t) - \eta \sqrt{y_o^2 - y^2(t)} dy \\ &= \pi \eta k y_o^2 \end{aligned} \quad (26)$$

The total oscillation energy is calculated as the energy stored in the lossless component of the complex spring at maximum displacement (at that point kinetic energy is zero),

$$W_{\text{tot}} = \frac{1}{2} k y_o^2. \quad (27)$$

By combining Equations (26) and (27) the loss factor is defined as,

$$\eta = \frac{W_d / 2\pi}{W_{\text{tot}}}. \quad (28)$$

Thus the loss factor is a damping parameter, which is proportional to the fraction of energy dissipated within the complex spring during a cycle of steady-state oscillation.

Applying the expansion (21) to the complex stiffness expression (20), the loss factor for the piezo stack is found to be,

$$\eta = \frac{\kappa^2 \omega C z_L}{1 + (1 - \kappa^2) (\omega C z_L)^2}. \quad (29)$$

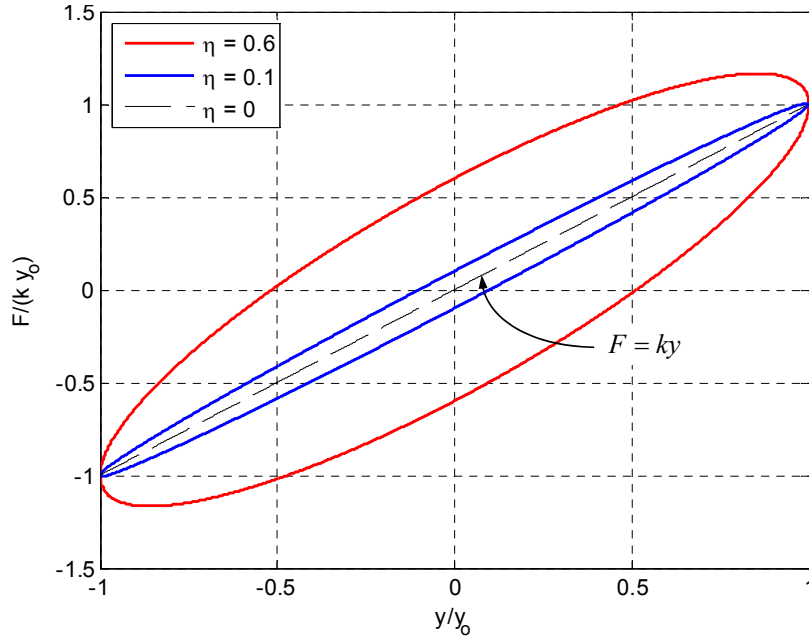


Figure 22.—Example force vs. displacement cycles based on Equation (25).

The expression shows that the loss factor is frequency dependent and its magnitude is affected by choice of load impedance. For the limited case of resistive loads, the equation $\partial\eta/\partial R_L = 0$ is solved to find the value that maximizes the loss factor,

$$R_L^{\max} = \frac{1}{\omega C \sqrt{1 - \kappa^2}}. \quad (30)$$

By inserting Equation (30) back into Equation (29), the maximum value for the loss factor is expressed as,

$$\eta^{\max} = \frac{\kappa^2}{2\sqrt{1 - \kappa^2}}. \quad (31)$$

This equation shows that the maximum loss factor is completely determined by the coupling coefficient.

In the design work implemented using this stack model, Equations (30) and (31) are used to select the stack and associated load resistance values that maximize the loss factor in specific frequency bands. Then Equation (20) is used to represent the stack as a complex spring element within the vibration ring mechanical framework. The system is simulated to produce the steady state vibration response of the vibration ring, and the corresponding forces transferred to the stack. Finally, the stack forces are used to calculate the current, voltage, and dissipated power using Equations (13) to (15).

There is a set of five stack parameters used in the model, $\{\kappa, d_{\text{eff}}, C, k_{\text{sc}}, k_{\text{oc}}\}$. Three of these should be determined from data, and the remaining two computed based on the linear relationships in Equations (18) and (19). As indicated by Table 3, the parameters may be determined based on element properties or stack measurements. Element properties are often available from manufacturer data sheets making them convenient to use. However, the equations relating element properties to stack parameters require several simplifying assumptions (those listed in Table 2, row 5). It's therefore preferable to use direct stack measurements to derive the model parameters. Table 3 shows the required stack measurements, though standard data collection methods do not exist at this time.

TABLE 3.—OPTIONS FOR DETERMINING THE STACK MODEL PARAMETERS

Via	Stack model parameters				
	κ	d_{eff}	C	k_{sc}	k_{oc}
Element properties ^a	κ_{el}	$n \cdot d$	$\frac{nA\epsilon^T}{l}$	$\frac{A}{nls^E}$	
Stack measurements ^a	$\frac{W_1}{W_1 + W_2}$	$\left. \frac{\Delta y}{\Delta V} \right _{F=0}$ or $\left. \frac{\Delta I / j\omega}{\Delta F} \right _{V=0}$	$\left. \frac{\Delta I / j\omega}{\Delta V} \right _{F=0}$	$\left. \frac{\Delta F}{\Delta y} \right _{z_L=0}$	$\left. \frac{\Delta F}{\Delta y} \right _{z_L=\infty}$

^aParameters based on element properties require the extra set of assumptions listed in Table 2, row 5. It's therefore more accurate to determine parameters from stack measurements.

TABLE 4.—SCOPE AND ASSUMPTIONS OF THE VIBRATION RING MODEL

1	Waveforms are represented by phasors to be consistent with the stack model.
2	Only radial force excitation is considered.
3	Deformation is assumed to be local, such that a 2D model represents the response of a finite circumferential section of the vibration ring.
4	Kinematic motion of the compression cage is modeled using rigid links (fixed length) that rotate about pin joints.
5	The effective cage stiffness, k_{cage} , is assumed to be linear. Linearity permits the use of superposition to incorporate the stack stiffness, \tilde{k} , into the compression cage framework.
6	The effective cage stiffness in the y-direction is assumed to be negligible in comparison to the piezo stack stiffness, \tilde{k} .
7	The compression cage stiffness ratio, α , is assumed to be independent of the link angle, so that it can be used as an input variable.
8	Inertial forces are not considered.

3.2 Vibration Ring Model

Using the complex spring representation of a shunted piezo stack, developed in the previous section, a 2D mechanical model of the vibration ring is developed. First, kinematic relationships of the compression cage are written, relating external compression to compression of the piezo stack. Springs are then introduced to represent the bending resistance of the compression cage as well as the complex stack stiffness. Free body analysis leads to a system of equations to predict the response of the vibration ring to vibratory excitation. These equations are then linearized to represent the vibration ring by its stiffness and loss factor parameters. These parameters are defined in relationship to the stiffness and loss factor of the piezo stack. The model is developed using the scope and assumptions listed in Table 4.

Figure 23 shows a cross sectional drawing of one of the more mature vibration ring design concepts (Con11a), both in its unloaded and loaded state. In this design, the compression cage is made of several butterfly amplifier segments, each paired with a discrete piezo stack. It should be noted that the model developed here may be applied to a design that uses a single ring-shaped stack by assuming that each amplifier segment is supported by a section of the stack circumference with associated stiffness, \tilde{k} . The figure has line segments superimposed to show the important dimensions of the compression cage. The geometric variables that change under load are shown with subscripts ‘unload’ and ‘load’ to indicate their state. The link and wall lengths do no change under load, and are defined by the following two equations.

$$L_{\text{link}} = \frac{x_{\text{unload}} - w}{2 \cos \phi_{\text{unload}}} \quad (32)$$

$$L_{\text{wall}} = y_{\text{unload}} + (x_{\text{unload}} - w) \tan \phi_{\text{unload}} \quad (33)$$

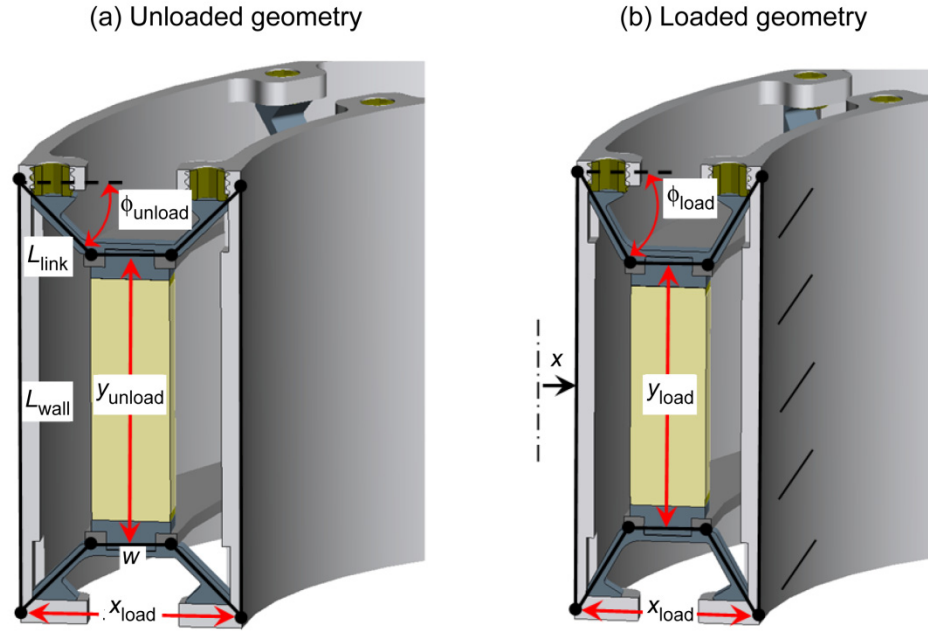


Figure 23.—Vibration ring model geometry based on Con11a. (a) Unloaded, (b) Loaded.

The motions of the compression cage are described by the following set of equations. The equations indicate that horizontal compression, x , increases the link angle, ϕ , which in-turn increases vertical compression, y' .¹

$$x_{\text{load}} = x_{\text{unload}} - x \quad (34)$$

$$\phi_{\text{load}} = \cos^{-1} \left(\frac{x_{\text{load}} - w}{2L_{\text{link}}} \right) \quad (35)$$

$$y_{\text{load}} = L_{\text{wall}} - \sqrt{4L_{\text{link}}^2 - (x_{\text{load}} - w)^2} \quad (36)$$

$$y' = y_{\text{unload}} - y_{\text{load}} \quad (37)$$

Figure 24 shows a simplified dynamic model (Fig. 24(a)) and corresponding free body diagrams (Fig. 24(b) and (c)). The complex stiffness, \tilde{k} , is included to represent either a shunted piezo stack or the load section of a shunted ring-shaped stack. In the simplified model, the walls and links are rigid and interconnected using pin joints. In reality the joints resist bending, which creates an effective stiffness in the horizontal and vertical directions. Here the vertical stiffness is neglected, because it is assumed to be small compared to the stack stiffness. The effective horizontal stiffness is captured by adding linear springs at the top and bottom, with combined stiffness k_{cage} . This value is also meant to include any other sources of cage resilience, such as the bending stiffness of the outer hoop. Based on the free body diagrams, the forces that arise due to compression of the structure are defined as follows.

¹ The prime reverses the sign convention. Primed variables therefore associate a positive sign with compression.

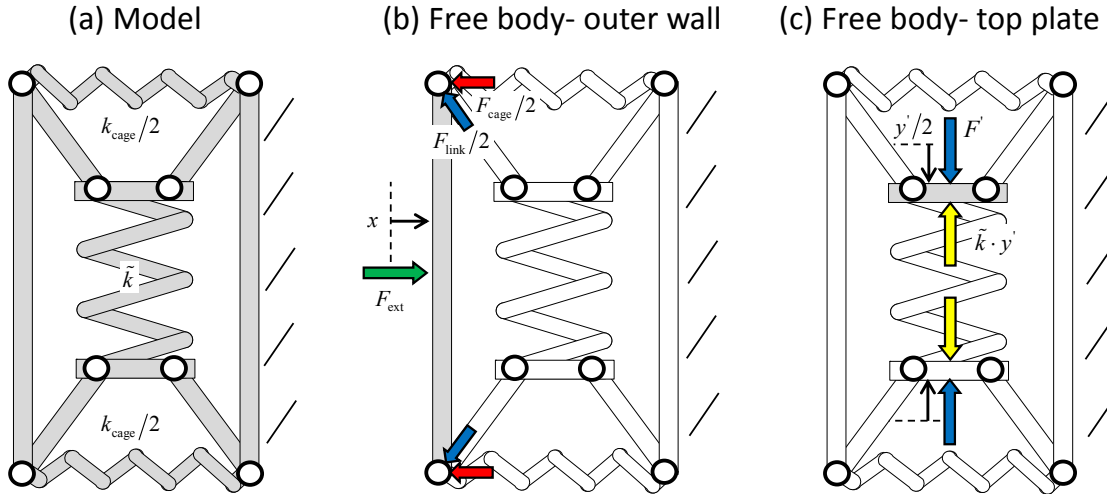


Figure 24.—Dynamic representation of vibration ring. (a) Lumped mechanical model, (b) Free body diagram of outer wall, (c) Free body diagram of stack top plate.

$$F' = \tilde{k} \cdot y' \quad (38)$$

$$F_{\text{cage}} = k_{\text{cage}} \cdot x \quad (39)$$

$$F_{\text{link}} = \frac{F'}{\sin \phi_{\text{load}}} \quad (40)$$

Summing the forces on the outer wall provides the following equation for the external force.

$$F_{\text{ext}} = F_{\text{cage}} + F_{\text{link}} \cos \phi_{\text{load}} \quad (41)$$

The set of equations will now be combined and linearized to produce expressions for the complex vibration ring stiffness as well as the transfer of external force to the stack. Combining Equations (32) to (41) provides the following expression for the complex stiffness,

$$\tilde{k}_{\text{vr}} := \frac{F_{\text{ext}}}{x} = k_{\text{cage}} + \tilde{k} \cdot G(\phi_{\text{unload}}) \quad (42)$$

The function G , expanded below, relates the complex stack stiffness to the complex vibration ring stiffness.

$$G = \frac{(x_{\text{unload}} - x - w)}{x} \left[1 - \frac{(x_{\text{unload}} - w) \tan \phi_{\text{unload}}}{\sqrt{\frac{(x_{\text{unload}} - w)^2}{\cos^2 \phi_{\text{unload}}} - (x_{\text{unload}} - x - w)^2}} \right] \quad (43)$$

Strictly speaking the value of G is dependant on the deformation response, x , and so it's a nonlinear term. However, by assuming that the value of G changes negligably with x , the following linear approximation may be used. Note that this approximation was derived by evaluating G at $x = 0$, applying L'hospital's rule, and limiting the domain to (0,90) degrees.

$$G = 1 + \frac{\cos 2\phi_{\text{unload}}}{\sin^2 \phi_{\text{unload}}} \quad (44)$$

Figure 25(a) shows the exact G function plotted over a practical range of deformation and for several different unloaded link angles. The function at $x = 0$ represents the estimate. The plot shows that the value of G deviates only slightly as x is increased. Figure 25(b) shows the complex stiffness using the estimate of G . Note that the results are shown normalized to the exact value of complex stiffness, and that k_{cage} has been set to zero as a worst case condition. The plots show that stiffness is overestimated by less than 1 percent, except when the link angle is lower than 35° .

Using the linear approximation for G , the vibration ring is treated as a complex-valued linear spring and expanded into its lossless stiffness component and loss factor according to Equation (2). Using this expansion as well as the equivalent stack stiffness expansion (21), the expression for complex vibration ring stiffness (42) is rewritten as,

$$k_{\text{vr}}(1 + j\eta_{\text{vr}}) = k_{\text{cage}} + k(1 + j\eta) \cdot G(\phi_{\text{unload}}). \quad (45)$$

By rearranging the real part of this equation, the following expression for stiffness is found.

$$k_{\text{vr}} = k \cdot G(\phi_{\text{unload}}) + k_{\text{cage}} \quad (46)$$

Then by defining the stiffness ratio,

$$\alpha = \frac{k_{\text{cage}}}{k_{\text{vr}}}, \quad (47)$$

the equation for vibration ring stiffness is simplified to,

$$k_{\text{vr}} = \frac{k \cdot G(\phi_{\text{unload}})}{1 - \alpha}. \quad (48)$$

By rearranging the imaginary part of Equation (45) the expression for the vibration ring loss factor is found to be,

$$\eta_{\text{vr}} = \frac{kG(\phi_{\text{unload}})\eta}{k_{\text{vr}}}. \quad (49)$$

Inserting Equation (48) reduces the expression to,

$$\eta_{\text{vr}} = (1 - \alpha)\eta. \quad (50)$$

Equations (48) and (50) show the basic relationships between the physical properties of the shunted stack and vibration ring. The vibration ring stiffness is proportional to the stack stiffness, with the proportionality constant (G) controlled by the link angle. As illustrated in Figure 26(a), different combinations of stack stiffness and link angle can be selected to produce the same target vibration ring stiffness. At low link angles, there is a stiffness magnification effect and therefore a very soft stack may be used. At high link angles, the opposite is true. Moreover, the vibration ring loss factor is proportional to that of the stack, and is not affected by the choice of link angle. Therefore, as illustrated in Figure 26(b), each of the stack-angle combinations that produce the same vibration ring stiffness has the same FT. The compression cage stiffness, as defined by α , has the effect of increasing the vibration ring stiffness, while decreasing the loss factor. It should be minimized to achieve maximize damping performance.

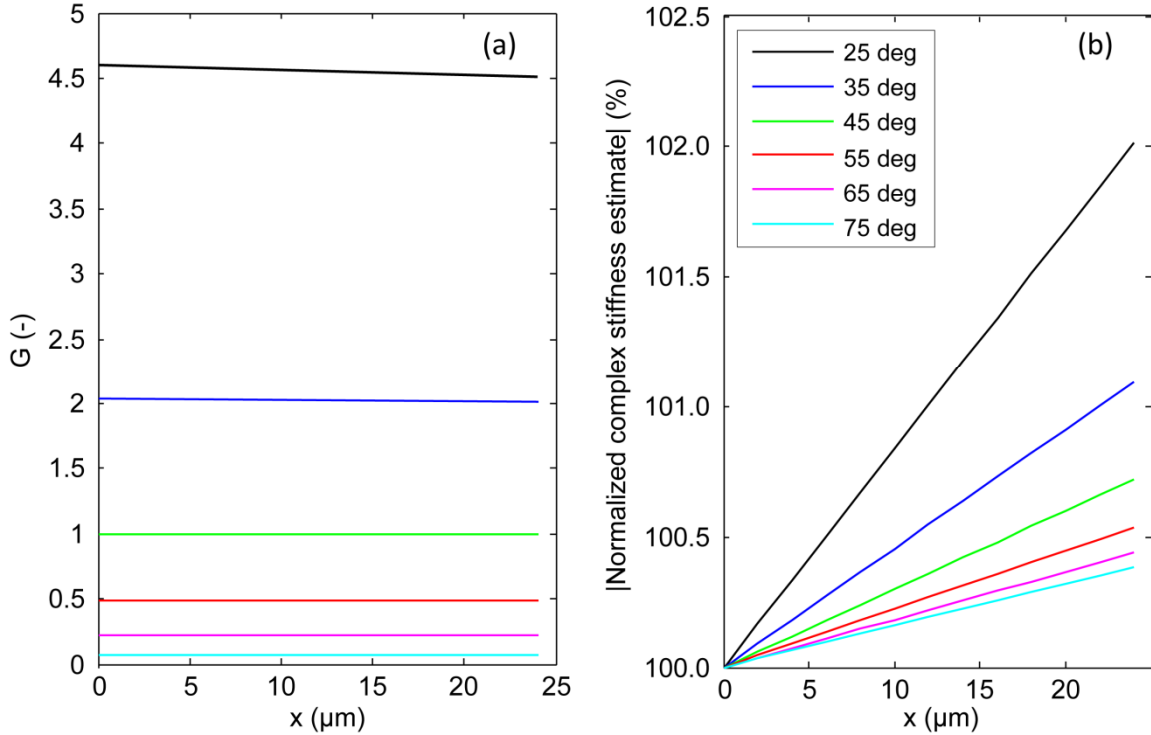


Figure 25.—Plots supporting linear approximation of G . (a) The G -parameter is shown to vary only slightly. (b) The resulting vibration ring stiffness is overestimated by less than 1 percent, except when the link angle is lower than 35° .

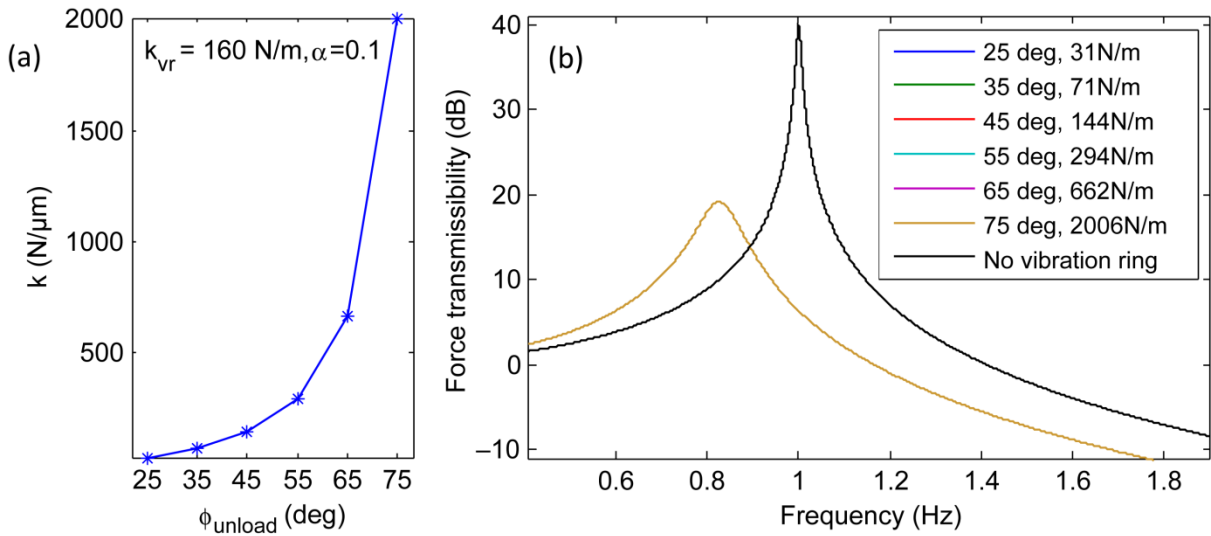


Figure 26.—Adjustability of the vibration ring. (a) Plot of link angle and stack stiffness combinations that produce the same vibration ring stiffness. (b) Simulation of simplified driveline (Eqs. (1) to (4)) showing that each combination produces the same force transmissibility.²

²The relationship shown is for constant stack stiffness, but the same idea applies when the stack stiffness is frequency dependent.

The following expression for compressive stack force is found by combining Equations (39) to (42),

$$F' = F_{\text{ext}} \tan \phi_{\text{load}} \left(1 - \frac{k_{\text{cage}}}{\tilde{k}_{\text{vr}}} \right). \quad (51)$$

This equation is also non-linear, as it depends on the response angle ϕ_{load} . The loaded link angle is replaced by the unloaded link angle to arrive at the following deterministic approximation.

$$F' = F_{\text{ext}} \tan \phi_{\text{unload}} \left(1 - \frac{k_{\text{cage}}}{\tilde{k}_{\text{vr}}} \right) \quad (52)$$

Figure 27(a) shows that the exact and estimated stack forces are very similar. Here $k_{\text{cage}} = 0$, as this produced the greatest deviation. Figure 27(b) shows the estimated stack force normalized to the exact value to better quantify the deviation. The data shows that stack force is underestimated by about 1 percent or less.

Rearranging the stack force estimate equation produces the force transfer ratio metric,

$$\text{FTR} = \frac{F'}{F_{\text{ext}} \tan \phi_{\text{unload}}} = 1 - \frac{k_{\text{cage}}}{\tilde{k}_{\text{vr}}}. \quad (53)$$

This equation is used to compare efficiency of transferring force to the stack. The equation also reveals that the cage stiffness essentially acts as a force shunt around the stack, which explains why reducing α increases the vibration ring loss factor.

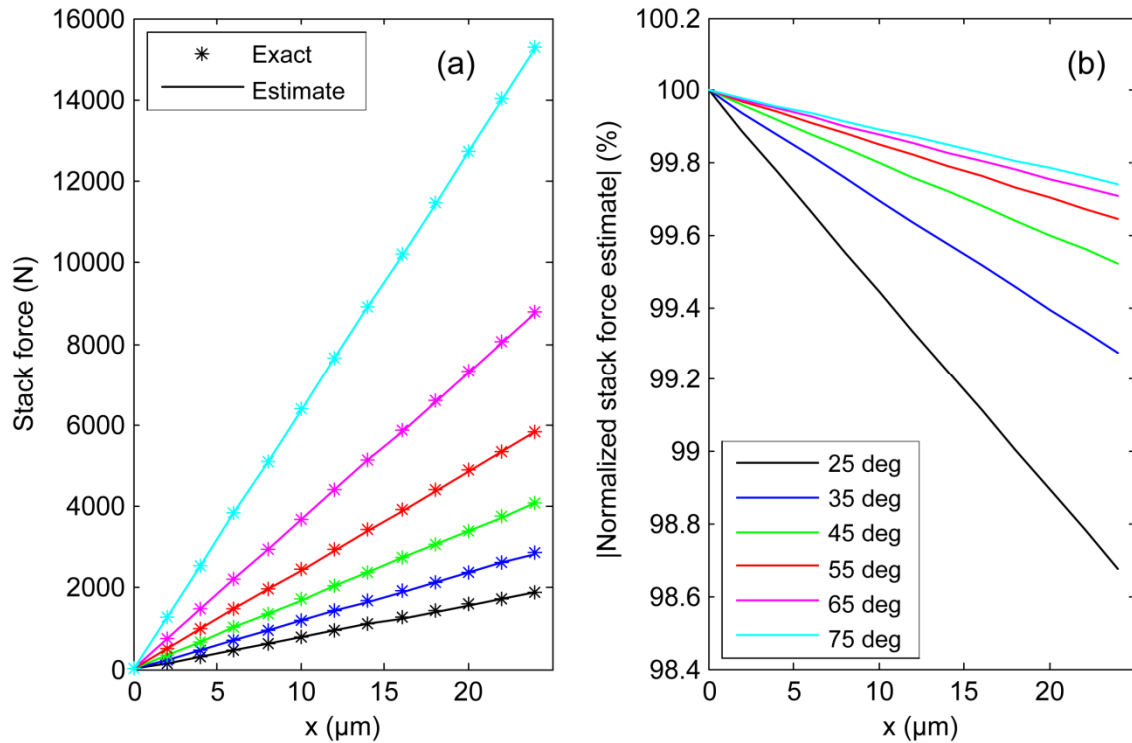


Figure 27.—Plots supporting linear approximation of F' . (a) The exact and estimated values are shown to be similar (b) Stack force is underestimated by about 1 percent or less.

Using the linearized equations, the vibration ring performance is completely defined by the stack parameters and the compression cage variables α and φ_{unload} . None of the other geometric variables are needed. The equations are used in two different linear combinations. In the next section, the stiffness and FTR equations are used to compare with static FEA results for Con10. Subsequently, the stack and model equations are used dynamically to determine how specific parameters influence damping.

3.3 Vibration Ring Finite Element Analysis

As a part of the design process, FEA models were developed for Con10 and 11. This was done to tune the stress distributions and optimize the FTR metric (53). As an example, Figure 28 shows the stress distribution from Con10b. In this section, the FEA model is examined in more detail and simulation results are compared with analytical model predictions.

The features and limitations of the analysis are listed in Table 5.

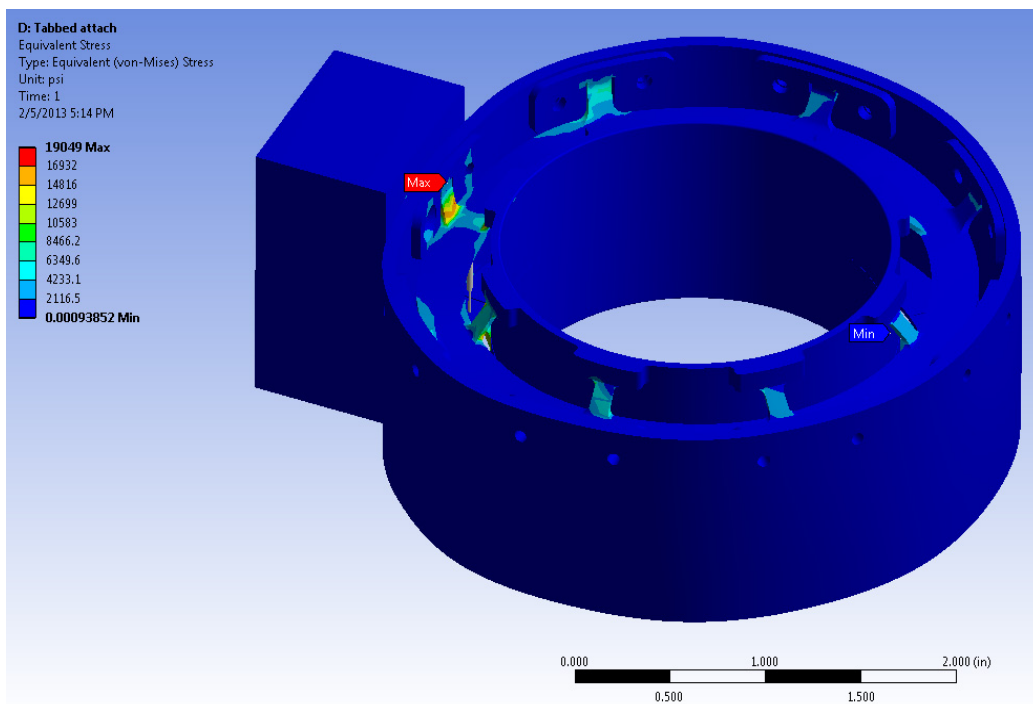


Figure 28.—Example FEA results showing stress distribution for Con10b.

TABLE 5.—FEATURES AND LIMITATIONS OF THE FINITE ELEMENT ANALYSIS

1	Only static analysis was implemented.
2	Stacks are represented by springs, and the spring force is spread over the contact area of the stack face.
3	Stack stiffness is real-valued, because loss factor is always zero for static loads.
4	Compression cage material properties are for stainless steel.
5	Assembly screws in Con10 are not represented explicitly. The mating surfaces are constrained to have matching displacements, moving as if bonded together.
6	Force is applied to the outer hoop with a flat rigid surface, as illustrated in Figure 28.
7	The inner hoop has fixed nodes so that it remains round.
8	Specific information regarding the prototypes is provided in the design section of this report.

Parametric study was conducted using the Con10b model following the steps in Table 6. Figure 29 provides further insight into how the model was tuned at each link angle. Given that the hoop diameters for Con10 and 11 were limited by the design specifications, changes in link angle were accommodated by changes in the link length. I.e. links were made to be longer when the angle was increased. As indicated by the procedure in Table 6, each design was tuned under a 400 N load by adjusting the radii and thickness dimensions shown in Figure 29 (R1-4 and T1-2). The first objective was to create even stack compression. To accomplish this, the inner links needed to be thinner and have smaller radii than the outer links. The second objective was to maximize the average stack compression, which is equivalent to maximizing the FTR as defined by Equation (53). This was a balance between establishing a rigid path for the force to transfer longitudinally through the links (resulting in high k_{vr}), while allowing the links to bend with little resistance (resulting in low k_{cage}). Clearly these were opposing goals with the present design concepts. The final objective was to minimize the maximum stress. Maximum stress was generally located within the link radii where the most bending occurred.

Static analysis was done with the analytical model for comparison with the FEA results. The calculation steps are listed in Table 7. Here the k_{cage} values were taken from the FEA results in order to highlight the other differences that exist between the models.

TABLE 6.—FEA PROCEDURE FOR PARAMETRIC STUDY OF CON10B

1	Select ϕ_{unload}
2	Set $F_{\text{ext}} = 400\text{N}$
3	Adjust the link geometry (radii R1-4 & thicknesses T1-2 from Figure 29) to achieve: <ul style="list-style-type: none"> • Even stack compression • Maximum average stack compression • Lowest maximum stress
4	Apply static forces up to 845 N and document x, F' , and maximum stress.* *Note that stack force was only recorded for 45°
5	Remove the stack springs and repeat step 4.
6	Compute the following $k_{\text{cage}} = \frac{F_{\text{ext}}}{x} \Big _{\text{stacks removed}}, k_{\text{vr}} = \frac{F_{\text{ext}}}{x}, \text{FTR} = \frac{F'}{F_{\text{ext}} \tan \phi_{\text{unload}}}$

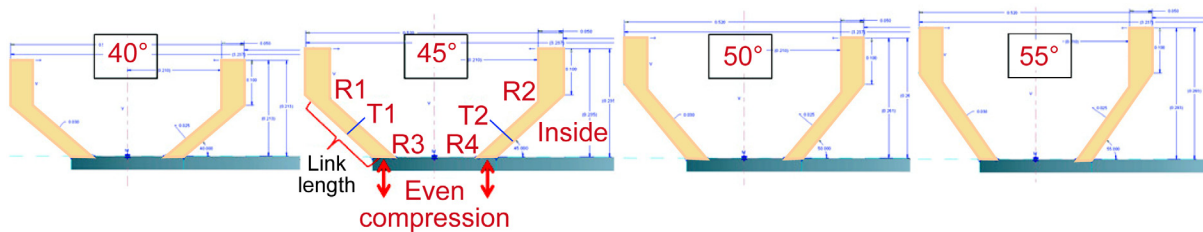


Figure 29.—Graphic to explain link geometry tuning procedure.

TABLE 7.—ANALYTICAL MODEL CALCULATION STEPS FOR COMPARISON WITH FEA

1	Input static parameters	$\frac{k_{\text{vr}}}{\text{constant}}, \frac{k_{\text{cage}}}{\text{from FEA}}, \frac{F_{\text{ext}} \cdot \phi_{\text{unload}}}{\text{Iterate}}$
2	Compute vibration ring stiffness	$G = 1 + \frac{\cos 2\phi_{\text{unload}}}{\sin^2 \phi_{\text{unload}}}, k_{\text{vr}} = k_{\text{cage}} + kG$
3	Compute stack force transfer ratio	$\text{FTR} = 1 - \frac{k_{\text{cage}}}{k_{\text{cage}} + kG}$

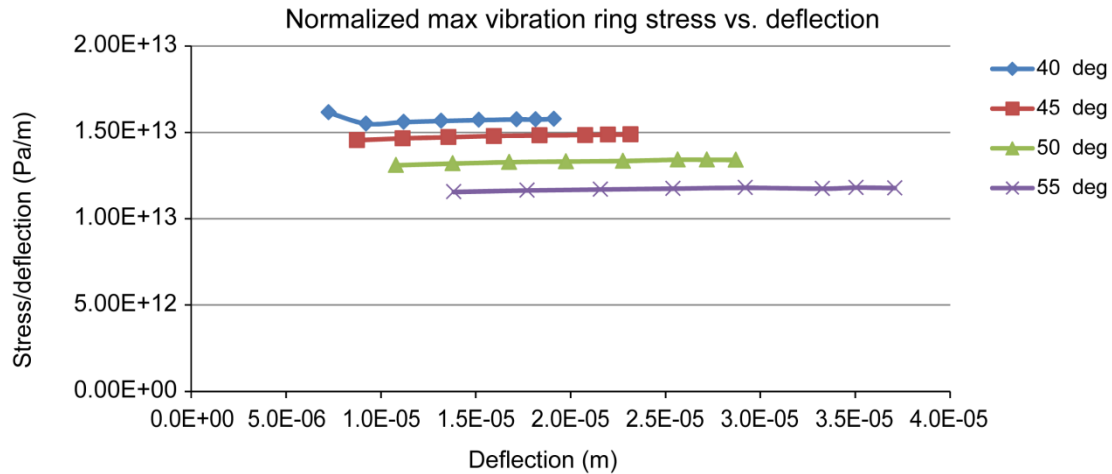


Figure 30.—FEA prediction of normalized maximum vibration ring stress vs. deflection.

3.3.1 Stress Analysis

The maximum stress associated with each design angle and loading condition is plotted in Figure 30 against deflection. The stress is normalized to deflection to allow for comparison between designs that have different stiffness. The flatness of the curves indicates that stress is a linear function of deflection for each design angle. Also, higher angle designs have lower normalized stress. This can be attributed to the increase in link length. For the same deflection, a longer link has less strain and therefore lower stress.

3.3.2 Evaluation of Analytical Model Assumptions

Several assumptions were made to develop the 2D analytical model. Each of the assumptions that relate to the mechanical response is evaluated here by examining the FEA results.

Assumption #3: Deformation is local

The assumption of local deformation was made so that the 2D model only needed to represent a single circumferential section of the vibration ring. For this to be valid, the 3D vibration ring response must only deform and experience stress in the vicinity of the applied load. Figure 31 shows exaggerated deformation patterns and stress distributions for Con10b and Con11b. Referring to Figure 31(a), most of the deformation in Con10 appears to be local. However, there is some noticeable hoop deformation outside of the loaded region. In addition, there is fairly significant stress in the links next to the loaded section. The wide mounting tabs appear to be increasing the bending stiffness of the hoop, causing the applied load to be distributed circumferentially. As shown in Figure 31(b), the results for Con11 are better. There is relatively little hoop deformation outside of the loaded region and minimal stress in the neighboring links. Despite the differences between these designs, the assumption of local deformation is considered to be reasonable.

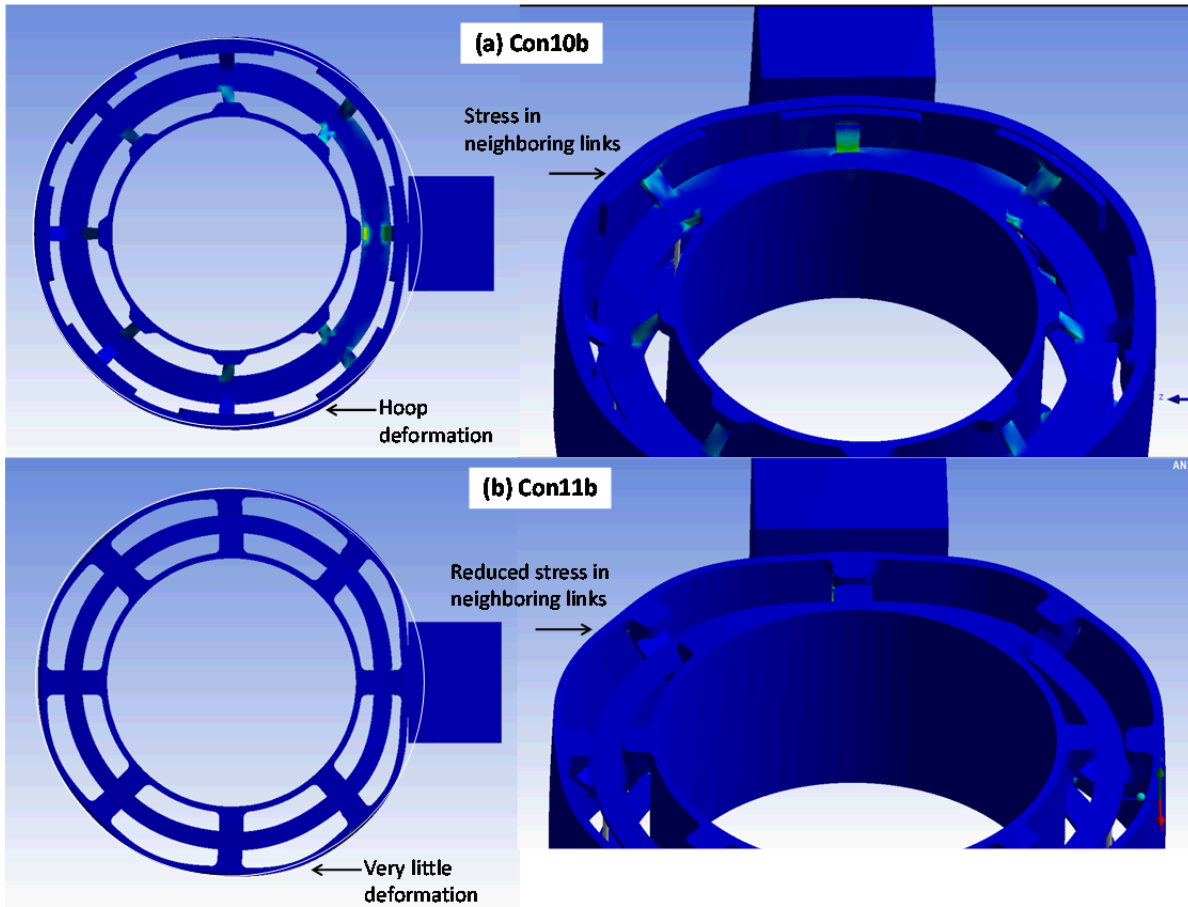


Figure 31.—Deformation patterns and stress distributions in vibration ring FEA models. (a) Con10b, (b) Con11b.

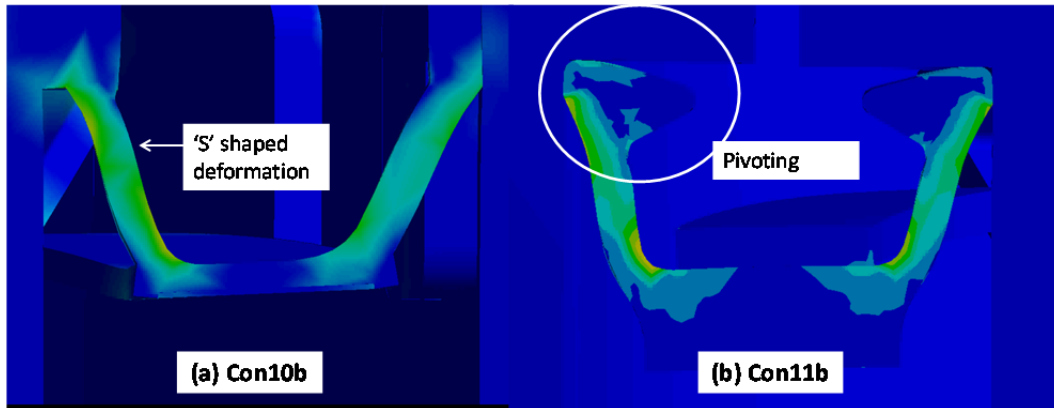


Figure 32.—Deformation patterns and stress distribution in links. (a) Con10b, (b) Con11b.

Assumption #4: Links are rigid

In the analytical model, the links were assumed to bend at the hinge locations but remain rigid in-between. Plots of the FEA deformation and stress patterns are shown in Figure 32. The link pattern of Con10b, shown in Figure 32(a), is shaped like an ‘S’. Rather than bending only at the hinge locations it bends globally. There is less deformation within the links of Con11b, as shown in Figure 32(b), but the links pivot at the top. Neither deformation pattern completely matches the assumption.

Given this discrepancy, there was a concern that the links may be softening the force transfer path between the vibration ring and stacks. FEA simulation was done with Con10b and Con11b where the stacks were made to be completely rigid. This enabled a measurement of stiffness, called blocking stiffness, which was associated with the link deformation. As shown in Table 8, the blocking stiffness was found to be on the same order of magnitude as the stack stiffness. This suggests that the links have a significant softening effect on the mechanism, which is not represented by the analytical model.

Assumption #5: Cage stiffness is linear

The linearity of k_{cage} is assumed when the stack spring, \tilde{k} , is inserted into the compression cage framework. This is an implicit use of the principal of superposition for linear systems. As a check of this assumption, the FEA model for Con10b was exercised with the stacks removed and the force and deflection were documented. The resulting cage stiffness curves for each design angle are shown in Figure 33 as a function of the applied force. It's apparent from the data that cage stiffness is quite linear.

Assumption #6: Alpha is independent of link angle

The parameter α was assumed to be independent of link angle, so it could be used as an input parameter in the analytical model. Recall that α is the ratio of cage stiffness to vibration ring stiffness. To evaluate the assumption, the FEA cage stiffness, vibration ring stiffness, and their ratio are shown in Figure 34 verses link angle for Con10b. Several loading conditions from 44 to 845 N are plotted here, but for the most part the curves lay on top of each other. Cage stiffness and vibration ring stiffness both decrease with link angle. However, they decrease at similar rates and their ratio remains constant at approximately 0.3. This suggests that the assumption is valid.

TABLE 8.—BLOCKING STIFFNESS COMPARED TO STACK STIFFNESS (Data collected from 45° models at 400 N)

	Stack (N/μm)	Blocking (N/μm)
Con10b	68	49
Con11b		60

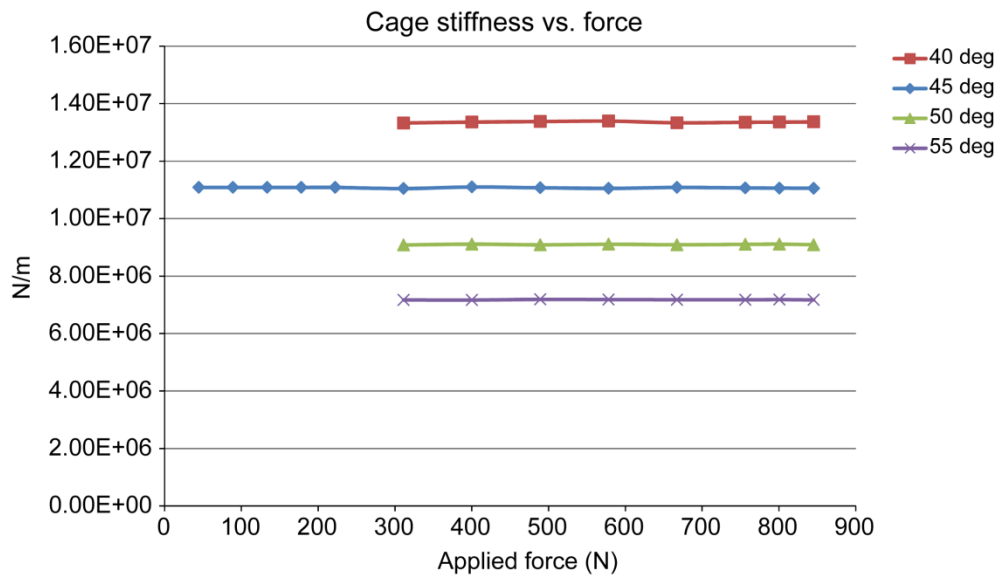


Figure 33.—FEA prediction of cage stiffness vs. force.

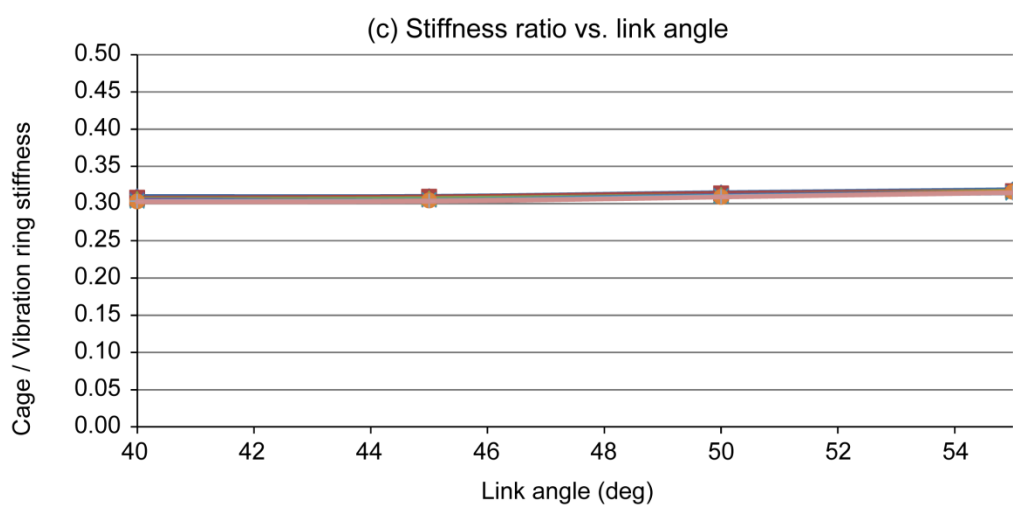
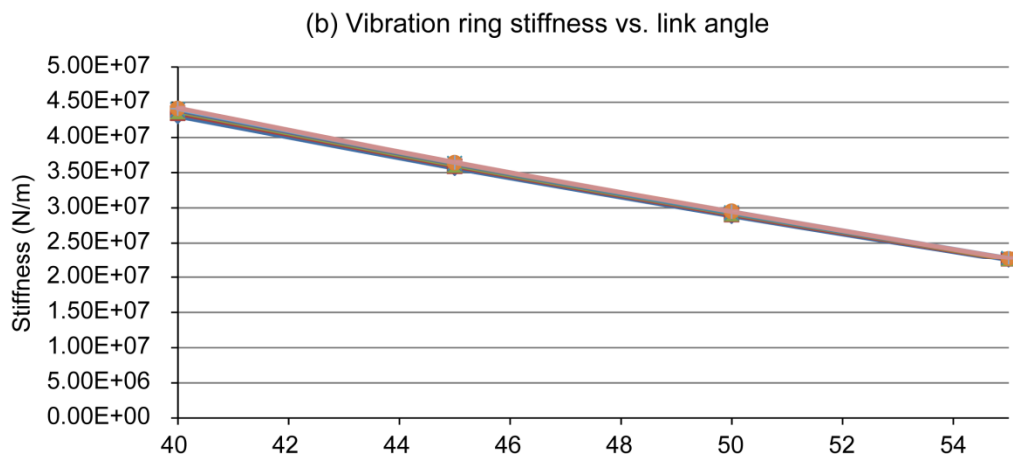
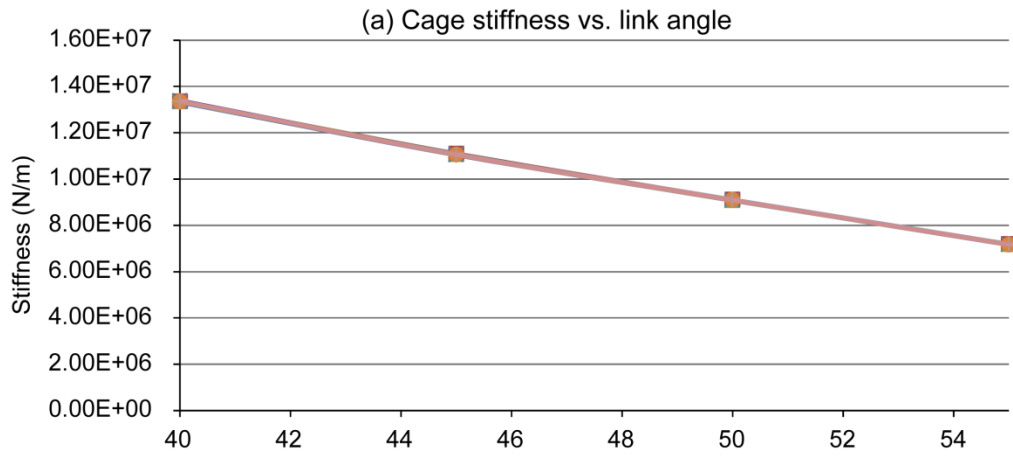


Figure 34.—FEA prediction of stiffness vs. link angle. (a) Cage stiffness, (b) Vibration ring stiffness, (c) Stiffness ratio.

3.3.3 Comparison With Analytical Model

Here the FEA predictions of vibration ring stiffness and FTR for the Con10b design are compared with the analytical model. Vibration ring stiffness versus link angle is plotted for all load cases in Figure 35. The bottom set of curves are the FEA results and the top set are the analytical results. The data shows that the analytical model significantly over-predicts the vibration ring stiffness, especially at the lower angles. Force transfer ratio data was only collected at 45°, and so it is plotted against applied force in Figure 36. The data shows that the analytical model also overestimates the FTR. It is hypothesized that these discrepancies are due to the assumption of rigid links being incorrectly applied in the analytical model. The analytical model should therefore be modified to represent the finite link stiffness.

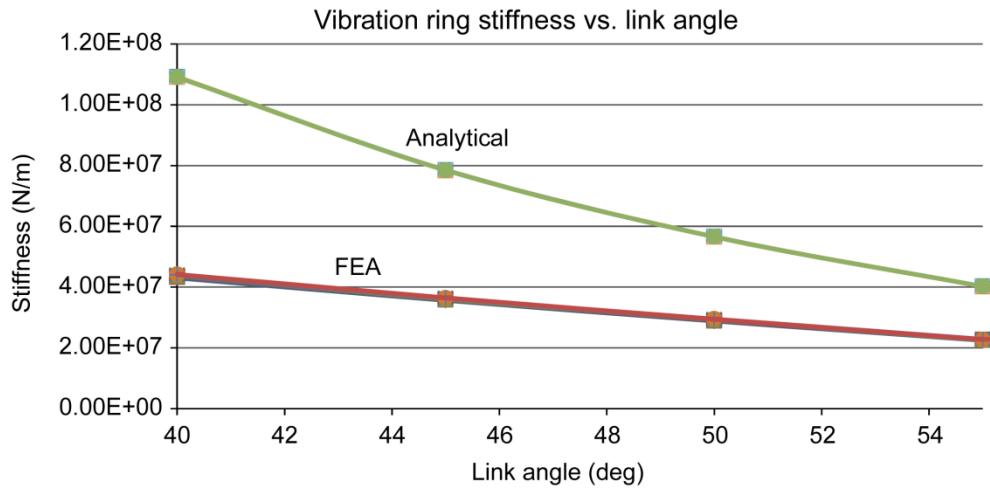


Figure 35.—FEA and analytical model predictions of vibration ring stiffness.

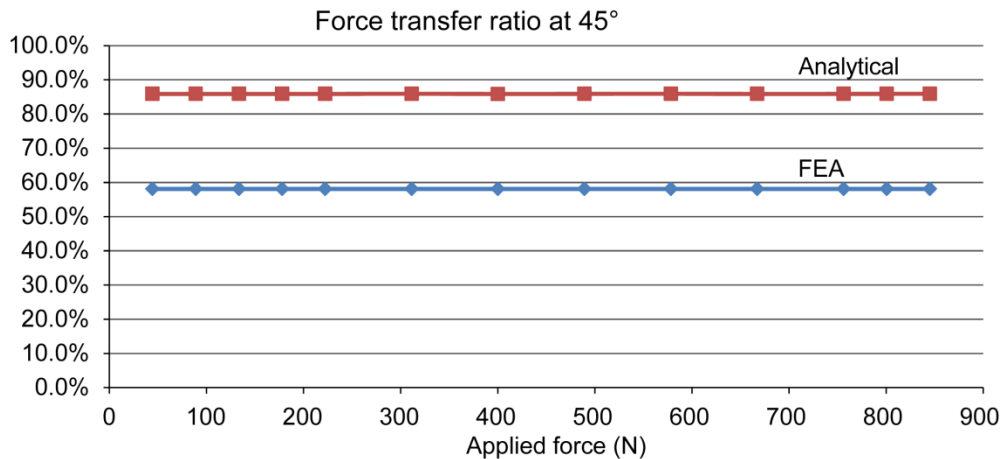


Figure 36.—FEA and analytical model predictions of force transfer ratio.

3.4 Driveline Damping Study Using Analytical Model

With an understanding of the strengths and limitations, the analytical model is used to study how the Vibration ring configuration affects driveline damping. The equations indicate that the parameter κ controls the peak loss factor of the stack (Eq. (31)), while α determines how much of the stack loss factor is reflected to the vibration ring (Eq. (50)). To understand the relative influence of these damping related parameters, a numerical study is done using the driveline model of Figure 2 (Eqs. (1) to (4)). Several vibration ring configurations are created by iterating κ and α through realistic ranges. Each configuration is simulated in the driveline model to compare damping performance. The calculation steps are listed in Table 10, and summarized in the text below.

The process starts by assigning several input parameters, including α , κ , the link angle, and β . The link angle is set to 45° , but as discussed in the previous section, from a conceptual design perspective this has no influence on the properties or performance of the vibration ring. Of course, selection of the link angle will influence details of the design. For example, it changes the stack stiffness needed to achieve a specific value for vibration ring stiffness.

TABLE 10.—CALCULATION STEPS FOR DRIVELINE DAMPING STUDY^a

1	Input	$\underbrace{F_{in}, f_{n,b}, k_b, \eta_b, \beta, \phi_{unload}}_{\text{Constant}} \quad \underbrace{f, \kappa, \alpha}_{\text{Iterate}}$
2	Calculate system information	$m_s = \frac{k_b}{(2\pi f_{n,b})^2}, \tilde{k}_b = k_b(1 + j\eta_b)$
3	Set vibration ring stiffness to create specific frequency shift.	$f_n = \beta f_{n,b}, k_{eff,n} = m_s(2\pi f_n)^2, k_{vr,n} = \frac{k_b k_{eff,n}}{k_b - k_{eff,n}}$
4	Set RC combination to maximize loss factor at new natural frequency.	$R_L^{\max} C = \frac{1}{2\pi f_n \sqrt{1 - \kappa^2}}, \eta^{\max} = \frac{\kappa^2}{2\sqrt{1 - \kappa^2}}, \eta_{vr}^{\max} = (1 - \alpha)\eta^{\max}$
5	Relate vibration ring stiffness to stack stiffness at new natural frequency.	$G = 1 + \frac{\cos 2\phi_{unload}}{\sin^2 \phi_{unload}}, k_n = \frac{(1 - \alpha)k_{vr,n}}{G}$ $H_n = 1 + \frac{\kappa^2}{1 - \kappa^2 + 1/j2\pi f_n R_L^{\max} C}, k_{sc} = \frac{k_n}{\text{Re}\{H_n\}}$
6	Compute complex stiffness spectra	$k_{cage} = \alpha k_{vr,n}, H = \left[1 + \frac{\kappa^2}{1 - \kappa^2 + 1/j2\pi f_n R_L^{\max} C} \right], \tilde{k} = k_{sc} H$ $\tilde{k}_{vr} = k_{cage} + \tilde{k}G, \tilde{k}_{eff} = \frac{\tilde{k}_b \tilde{k}_{vr}}{\tilde{k}_b + \tilde{k}_{vr}}$
7	Compute driveline performance spectra	Dynamic compliance: $c = \frac{x_s}{F_{in}} = \frac{1}{-(2\pi f)^2 m_s + \tilde{k}_{eff}}$ Force transmissibility: $FT = c \cdot \tilde{k}_{eff}$
8	Compute forced response spectra	Force on vibration ring: $F_{ext} = F_{out} = F_{in} \cdot FT$ Stack force: $F' = F_{ext} \tan \phi_{unload} \left(1 - \frac{k_{cage}}{\tilde{k}_{vr}} \right)$ Electrical power: $P_L = \frac{\kappa^2 (-F')^2}{k_{sc} \left(1 + 1/j2\pi f_n R_L^{\max} C \right)^2 R_L^{\max} C}$

^aVariables defined at the natural frequency have the subscript n

The β parameter defines the natural frequency reduction that the driveline system can tolerate when the vibration ring is integrated. Reduction in natural frequency is associated with softening of the vibration ring. This improves the system damping performance, but the allowable shift is generally constrained by the operating frequencies of the machine. Therefore the selection of β in practice will be system specific. Here a value of 0.8 (20 percent reduction) is arbitrarily selected for all simulation cases.

Using the value for β , the vibration ring stiffness is chosen using the formula for un-damped natural frequency in a single degree of freedom system. Then, the RC combination of the circuit and stack is selected with the purpose of maximizing damping at the new natural frequency. Next, the required short-circuit stiffness of the stack is found. Finally, the complete spectra of stack and vibration ring properties as well as driveline performance metrics are calculated.

3.4.4 Case 1: Variation of κ (piezo electromechanical coupling factor)

For simulation case 1, κ is iterated through the set $\{0.5, 0.7, 0.9\}$ while α is fixed. Note that 0.5 represents a very weak electromechanical coupling factor, 0.7 is typical of piezoceramic stacks, and 0.9 is typical for single-crystal piezo stacks. Figure 37 shows the spectra of stack and vibration ring properties. Here the dashed vertical line indicates the predicted new natural frequency after the vibration ring is integrated with the driveline. As intended, the vibration ring stiffness for each case is identical at the natural frequency. However, the frequency dependence of vibration ring stiffness increases with κ . For example, the configuration with largest κ has both the lowest DC stiffness and the highest stiffness at the maximum frequency. The stack stiffness follows the same trends as the vibration ring stiffness, but its magnitude is slightly smaller due to the finite value of α .

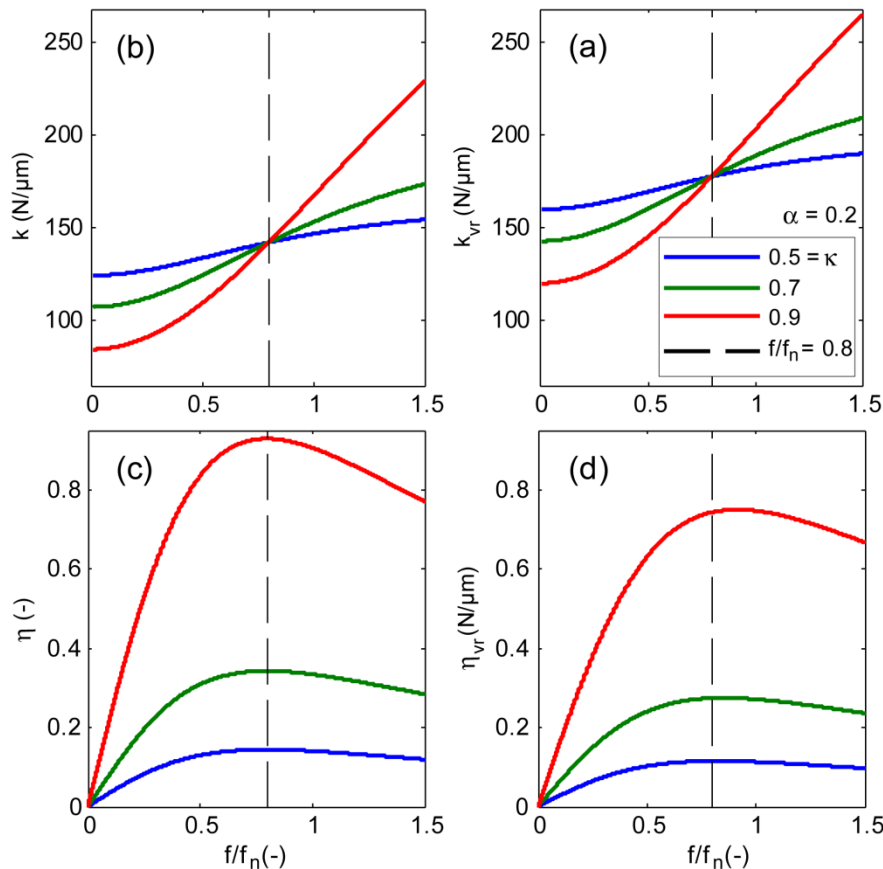


Figure 37.—Influence of κ on property spectra (simulation case 1). (a) Vibration ring stiffness, (b) Stack stiffness, (c) Stack loss factor, (d) Vibration ring loss factor.

As expected, the stack loss factor peaks at the natural frequency and drops to zero at DC. The vibration ring loss factor follows the same trends, though the absolute values are 80 percent less due to the finite value of α . Changes in κ appear to have a profound effect on the vibration ring loss factor. For example the change from $\kappa = 0.7$ to 0.9 causes a 270 percent increase in the loss factor peak. This drastic improvement motivates the use of single-crystal piezo stacks over piezoceramic stacks.

The driveline system performance for simulation 1 is shown in Figure 38. In the FT plot, the natural frequency was shifted to the target location for the lower two cases of κ . However, at the highest value of κ the natural frequency is slightly greater. This is because the calculations were based on the formula for un-damped natural frequency, which is imprecise for heavily damped systems. The calculation procedure may be considered conservative, since the natural frequency was shifted to a larger value than planned.

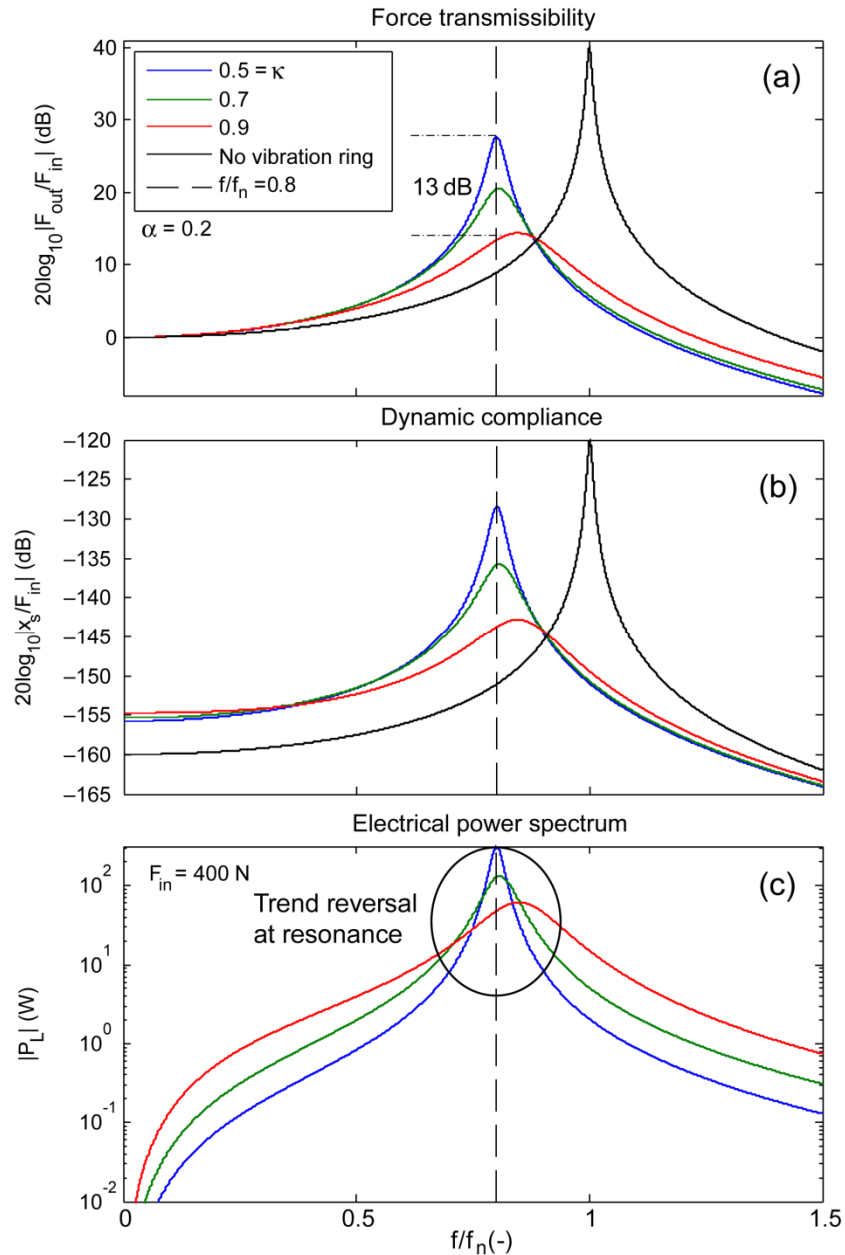


Figure 38.—Influence of κ on driveline system performance spectra (simulation case 1). (a) Force transmissibility, (b) Dynamic compliance, (c) Electrical power.

For all cases the reduction in peak FT response was significant, on the order of 10's of dB. Note that the exact reduction in peak FT is not relevant, because the driveline damping parameters (with no vibration ring) were selected arbitrarily. The variation in peak FT between the cases was significant, 13 dB, supporting the notion that κ is a critical parameter. Reduction in peak FT is directly related to the peak loss factor, indicating that loss factor is an appropriate metric for evaluating the vibration ring's potential damping performance.

The trends in dynamic compliance around the natural frequency are nearly identical to the FT, which indicates that a vibration ring design that reduces transmitted force will concurrently suppress the motion of the shaft at resonance. On the other hand, the trends for power generation are unique. Below and above the resonance the power generated is directly related to κ . This is expected, because stacks with higher κ convert more of the applied mechanical energy to electrical energy. Around the resonant peak, however, the trend reverses; as κ is increased less power is generated. I.e. when the resonance is dampened, less work is done on the vibration ring and therefore less power is generated. To make use of the generated energy, of course, the resistive load would need to be replaced by an energy harvesting circuit with the desired impedance.

3.4.5 Case 2: Variation in α (Stiffness Ratio)

For simulation case 2, the influence of cage stiffness is studied. The ratio of cage stiffness to overall vibration ring stiffness, parameter α , is iterated through the set $\{0.3, 0.2, 0.1\}$ while κ is fixed. The range for α was selected based on the intuition gained after creating several compression cage designs. The highest value is meant to correspond to a preliminary design and the lowest value represents an optimized design. Note that for a compression cage that transmits significant torque, the value of α may be higher than 0.3. Figure 39 shows the spectra of stack and vibration ring properties, while Figure 40 shows the driveline performance spectra. Note that the green line in these plots represents the same configuration ($\kappa = 0.7$, $\alpha = 0.2$) as the green line in the simulation case 1 plots.

Considering first the vibration ring stiffness, the change in frequency dependence for the different cases is relatively small and therefore the variation in DC stiffness is minor. The stack stiffness curves are shifted vertically according to the differences in cage stiffness with each design. I.e. when α is reduced it requires a slightly higher stack stiffness to achieve the target vibration ring stiffness. For all three cases, the stack loss factor spectra are the same. This is because each case has the same κ (stack type) and is optimized to the same frequency. However, higher values of α lead to lower vibration ring loss factor. As mentioned previously, the cage stiffness acts as a force shunt reducing the influence of the stack. The resulting changes in vibration ring loss factor are significant, but much less than the changes observed through variation of κ . Therefore, α should be considered a secondary design factor with regard to damping.

All of the trends in driveline performance, shown in Figure 40, are consistent with simulation 1. Increases in loss factor, created by reducing alpha, correspond to reductions in the peak FT. Here, the peak FT only varies by 2 dB as the variation in loss factor is minor. The dynamic compliance around the resonance follows the same trends as FT, supporting the idea that the vibration ring simultaneously reduces transmitted force and shaft motion. Considering the power spectra, the vibration ring with the best damping performance generates the most power above and below resonance, but the trend reverses close to the peak.

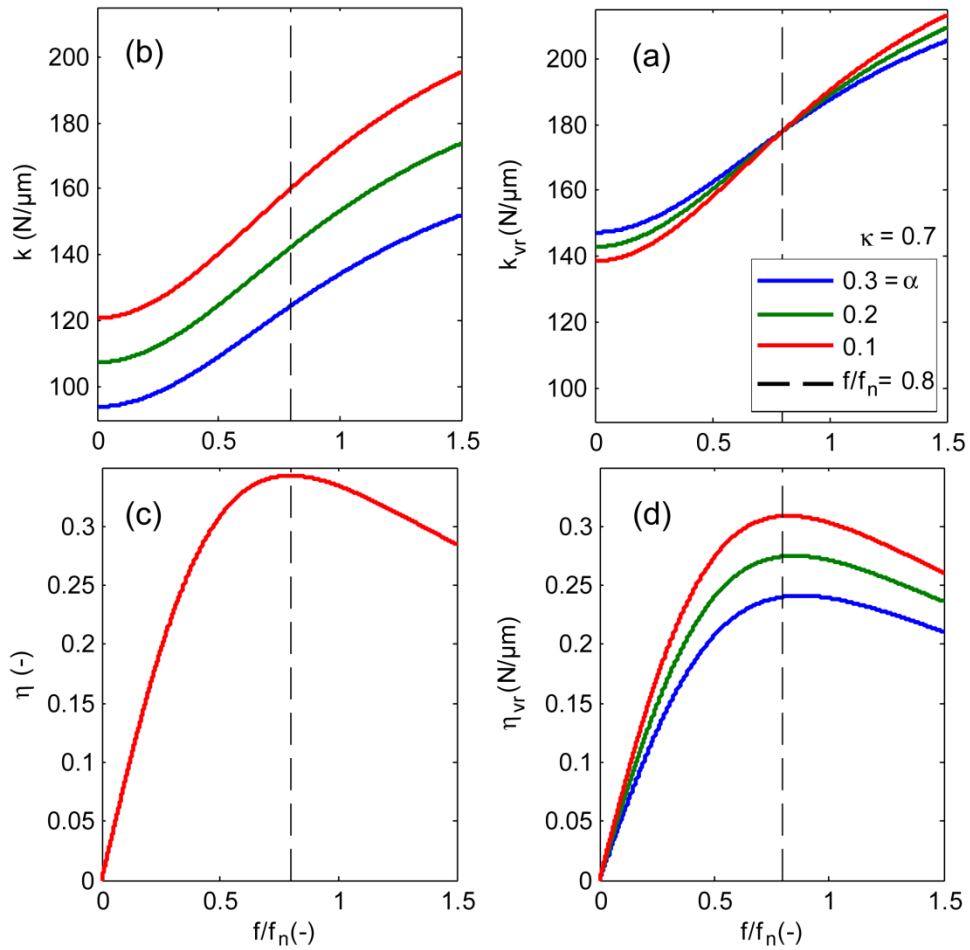


Figure 39.—influence of α on property spectra (simulation case 2). (a) Vibration ring stiffness, (b) Stack stiffness, (c) Stack loss factor, (d) Vibration ring loss factor.

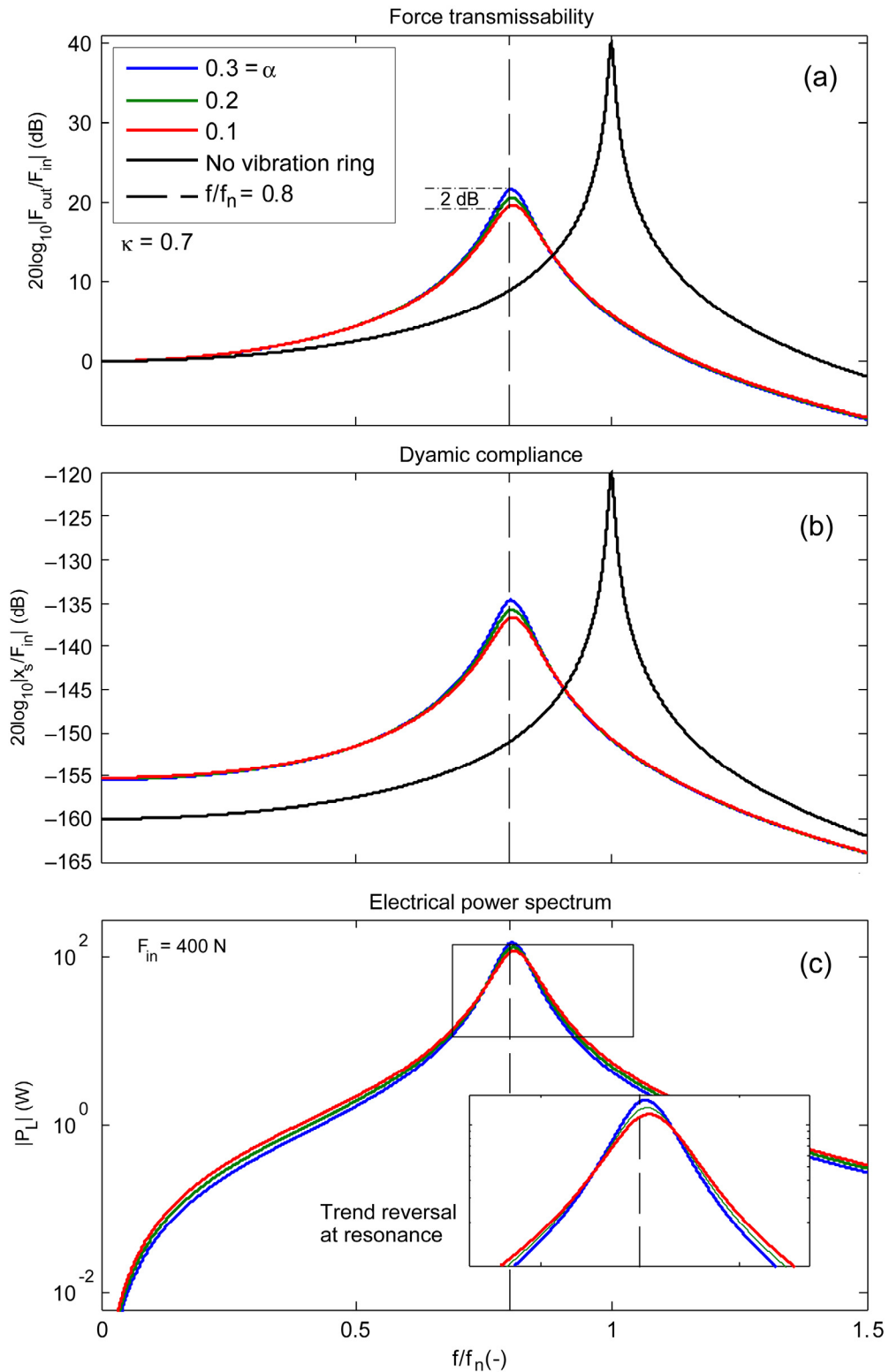


Figure 40.—Effect of α on driveline system performance spectra (simulation case 2). (a) Force transmissibility, (b) Dynamic compliance, (c) Electrical power.

4.0 Conclusion

4.1 Summary

Introduction: The vibration ring was conceived as a driveline damping device to prevent structure-borne noise in machines. It has the appearance of a metal ring, and can be installed between any two driveline components like an ordinary mechanical spacer. Damping is achieved using a ring-shaped piezoelectric stack that is poled in the axial direction and connected to an electrical shunt circuit. Surrounding the stack is a metal structure, called the compression cage, which squeezes the stack along its poled axis when excited by radial driveline forces. The stack in turn generates electrical energy, which is either dissipated or harvested using the shunt circuit. Removing energy from the system creates a net damping effect. The vibration ring is much stiffer than traditional damping devices, which allows it to be used in a driveline without disrupting normal operation. In phase 1 of this NASA Seedling Fund project, a combination of design and analysis was used to examine feasibility of this concept.

Design: Several design concepts were evaluated using solid modeling, finite element analysis, and by creating prototype hardware. Early concepts focused on developing a compression cage structure that could transfer radial force through the poled axis of the stack. The so called ‘segmented butterfly amplifier’ was found to provide the required kinematics. It used several mechanical amplifiers spaced around the circumference, which squeezed the piezo stack in the axial direction when the walls of the compression cage were moved closer together. Complete prototypes were made, using both additive and traditional manufacturing techniques. Additive designs had fewer parts and more straightforward assembly procedures, but the parts lacked the required precision. Designs based on traditional manufacturing were more precise, but they required several small parts and were cumbersome to assemble. To evaluate the damping properties and resulting power generation of the prototypes a load-frame test was developed. Test results will be reported in phase 2 of the project.

Analysis: Analytical modeling was used to evaluate the combined electro-mechanical response of a simplified cross-section of the vibration ring, while finite element analysis served to provide greater insight into the mechanical response of the detailed three-dimensional designs. In the analytical model the shunted stack was formulated as a complex-valued mechanical spring integrated within the mechanical framework of the butterfly amplifier. The model revealed that the stiffness and damping of the stack and overall vibration ring were related through the amplifier’s link angle and cage stiffness ratio parameters. Finite element analysis showed that the detailed designs did not exhibit ideal performance, because the amplifier links deformed under load. This reduced the mechanical coupling between the stack and vibration ring, thereby causing reductions in stiffness and loss factor of the mechanism. After comparison with the finite element model, the analytical model was used to evaluate how the vibration ring configuration affected damping in a simple driveline. The electromechanical coupling factor of the stack was shown to have an enormous influence on loss factor and the resulting driveline damping performance. The cage stiffness ratio of the vibration ring was somewhat influential, but much less than the coupling factor. Above and below the system resonance, power generation was shown to be directly related to damping. However, in the vicinity of the resonance less power was generated when damping was increased.

4.2 Lessons

The following lessons should be taken into consideration for continued development of this mechanism.

1. Considering the simulation results, the vibration ring should be stiffer than the other driveline components to prevent significant shifts in natural frequency, while the vibration ring loss factor should be made as high as possible to reduce peak force transmissibility.
2. The stiffness and loss factor of the vibration ring are proportional to the respective stiffness and loss factor of the shunted stack within. The compression cage link angle scales the stiffness, but does not affect the loss factor. The peak loss factor is mainly controlled by the electromechanical coupling factor of the stack, and the frequency of the peak is tuned by selecting the circuit impedance.
3. Configuring the vibration ring to reduce force transmissibility will also suppress shaft motion around resonance. However, as the resonant response is suppressed less power will be generated.
4. The segmented butterfly amplifier provides the required kinematic relationship, but has the following design challenges.
 - a. Its geometry requires significant axial width. Therefore future designs should compensate for this by using shorter stacks or by modifying the amplifier geometry.
 - b. To effectively transfer force through the stack, the links must be stiff, and the joints must bend freely. An alternative link design should be considered, which allows for the joints and links to be tuned separately.
5. Assembling the compression cage around a ring-shaped stack is not trivial. Concepts 8, 10a, and 11 each use different methods to solve this problem. The assembly methods of each design should be considered to develop the next concept iteration.
6. Additive manufacturing can reduce the number of cage parts making assembly more straightforward. The direct metal laser sintering process used for Con10b, however, had the unintended consequence of warping thin sections of the cage. Alternative additive processes should be tried.
7. Con11b demonstrated that the compression cage may be created using traditional manufacturing by using several individual parts. The required interference fit between the links and hoop walls make the structure difficult to assemble. Future multi-part designs should use a method to enable clearance between parts during assembly.

4.3 Plans for Phase 2

In phase 2, the vibration ring will be optimized for a specific application by the following process.

1. Determine target vibration ring properties (e.g., stiffness, loss factor, and frequency band) for a specific driveline application.
2. Find the properties of the existing vibration ring prototypes using the load frame test, in order to establish a baseline for improved performance and provide model validation data.
3. Update the analytical framework to include the effect of link deformation, and then validate the model using the load test data.
4. Using the model, define a vibration ring configuration (e.g., electromechanical coupling factor, circuit impedance, stack and cage stiffness, and link angle) that would have the desired properties.
5. Iteratively design, build, and test new concepts, based on the desired configuration, using the load frame test to evaluate properties.
6. Evaluate the most promising designs in the driveline application to determine damping performance.

References

- ANSI. (1987). *IEEE Standard on Piezoelectricity*. New York: The Institute of Electrical and Electronics Engineers, Inc.
- Atzrodt, H., Mayer, D., & Melz, T. (2009). Reduction of Bearing Vibrations with Shunt Damping. *16th International Congress on Sound and Vibration* (pp. 2383-2389). Krakow, Poland: Curran Associates, Inc.
- Davis, C.L., & Lesieutre, G.A. (2000). An Actively Tuned Solid-State Vibration Absorber Using Capacitive Shunting of Piezoelectric Stiffness. *Journal of Sound and Vibration*, 601-607.
- Hagood, N.W., & von Flotow, A. (1991). Damping of Structural Vibrations with Piezoelectric Materials and Passive Electrical Networks. *Journal of Sound and Vibration*, 243-268.
- National Science and Technology Council. (2010). *Security and Homeland Defense Goal #2, in the National Aeronautics Research and Development Plan*. Washington D.C.: Executive Office of The President.
- Ungar, E.E., & Kerwin Jr., E.M. (1962). Loss Factors of Viscoelastic Systems in Terms of Energy Concepts. *The Journal of the Acoustic Society of America*, 954-957.

